













Microbial iron cycling during palsa hillslope collapse promotes greenhouse gas emissions before complete permafrost thaw

Monique S. Patzner ¹, Merritt Logan ², Amy M. McKenna ³, Robert B. Young ^{2,4}, Zhe Zhou ^{1,5}, Hanna Joss¹, Carsten W. Mueller ^{6,7}, Carmen Hoeschen ⁶, Thomas Scholten ⁸, Daniel Straub ^{9,10}, Sara Kleindienst ⁹, Thomas Borch ², Andreas Kappler ^{1,11} & Casey Bryce¹²✉

Reductive dissolution during permafrost thaw releases iron-bound organic carbon to porewaters, rendering previously stable carbon vulnerable to microbial decomposition and subsequent release to the atmosphere. How mineral iron stability and the microbial processes influencing mineral dissolution vary during transitional permafrost thaw are poorly understood, yet have important implications for carbon cycling and emissions. Here we determine the reactive mineral iron and associated organic carbon content of core extracts and porewaters along thaw gradients in a permafrost peatland in Abisko, Sweden. We find that iron mineral dissolution by fermentative and dissimilatory iron(III) reduction releases aqueous Fe²⁺ and aliphatic organic compounds along collapsing palsa hillslopes. Microbial community analysis and carbon emission measurements indicate that this release is accompanied by an increase in hydrogenotrophic methanogen abundance and methane emissions at the collapsing front. Our findings suggest that dissolution of reactive iron minerals contributes to carbon dioxide and methane production and emission, even before complete permafrost thaw.

¹Geomicrobiology, Center for Applied Geosciences, University of Tuebingen, Schnarrenbergstrasse 94-96, 72076 Tuebingen, Germany. ²Department of Soil & Crop Sciences and Department of Chemistry, Colorado State University, 307 University Ave, Fort Collins, CO 80523-1170, USA. ³National High Magnetic Field Laboratory, Florida State University, Tallahassee, FL 32310-4005, USA. ⁴Chemical Analysis and Instrumentation Laboratory, New Mexico State University, P.O. Box 30001MSC 3RES, Las Cruces, NM 88003, USA. ⁵Alfred-Wegener-Institute, Helmholtz Centre for Polar and Marine Research, Am Handelshafen 12, 27570 Bremerhaven, Germany. ⁶Chair of Soil Science, TUM School of Life Sciences, Technical University of Munich, Emil-Ramann Strasse 2, 85354 Freising, Germany. ⁷Department of Geosciences and Natural Resource Management, University of Copenhagen, Øster Voldgade 10, 1350 Copenhagen, Denmark. ⁸Chair of Soil Science and Geomorphology, University of Tuebingen, Rümelinstraße 19-23, 72070 Tübingen, Germany. ⁹Microbial Ecology, Center for Applied Geosciences, University Tuebingen, Schnarrenbergstrasse 94-96, 72076 Tuebingen, Germany. ¹⁰Quantitative Biology Center (QBiC), University Tuebingen, Auf der Morgenstelle 10, 72076 Tuebingen, Germany. ¹¹Cluster of Excellence: EXC 2124: Controlling Microbes to Fight Infection, Tübingen, Germany. ¹²School of Earth Sciences, University of Bristol, Wills Memorial Building, Queens Road, Bristol BS8 1RJ, UK.

✉email: casey.bryce@bristol.ac.uk

Climate change has enormous consequences for permafrost environments, causing rapid changes in soil conditions (such as thermal and moisture regime, and aeration) with direct consequences for organic (OC) destabilization¹. Permafrost soils store ~60% of the world's soil OC in 15% of the global soil area^{2,3}. This preserved OC will become increasingly exposed to microbial decomposition and thus can be released from the active layer to the atmosphere as greenhouse gases (GHGs) such as carbon dioxide (CO₂) and methane (CH₄)⁴ or discharged by drainage⁵. However, the magnitude of the release of this OC depends strongly on a large variety of factors⁶, including the hydrology, soil parent material, organic matter content and the ability of soil minerals to protect OC from degradation, which can regulate long-term preservation of OC⁷.

Reactive iron (Fe) minerals (defined as the solid Fe phases that are reductively dissolved by sodium dithionite^{8–10}) have been shown to preserve OC over geological timescales in numerous environments^{7,9} and thus are considered as an effective rusty carbon sink¹¹. These Fe minerals are known to stabilize OC by sorption/co-precipitation and protect it from degradation by generating Fe-OC associations that are more persistent in soils^{9,12–16}. However, by providing a terminal electron acceptor for anaerobic respiration^{17,18}, Fe(III) minerals can also enhance OC decomposition and lead to CO₂ formation. The fate of Fe and associated OC determines Fe-OC aggregate formation and ultimately accessibility for microbial decomposition^{18–20}. Previous research has identified Fe-OC interactions in several permafrost environments (e.g.^{21–26}). It has been shown that reactive Fe minerals can bind 7 to 20% of total OC (TOC) in intact permafrost environments^{10,27}, but cannot preserve OC along a permafrost thaw gradient¹⁰. This Fe-bound carbon stock in intact permafrost environments, such as palsas underlain by intact permafrost, which becomes mobilized with permafrost thaw, is equivalent to between 2 and 5 times the amount of carbon released yearly through anthropogenic fossil fuel emissions¹⁰.

Palsas have been the focus of extensive research (e.g.^{28–32}), however, the stability of solid phase Fe-OC associations during transitional processes, such as palsa collapse into partially-thawed bogs, remain understudied. The need to better understand the climate impact of transitional processes in thawing permafrost was stated previously by Shelef et al.³³ who emphasize large uncertainty in permafrost carbon stocks (>200%) due to largely unidentified biogeochemical processes at collapsing fronts, which either lead to carbon sequestration or carbon release as greenhouse gases. Indeed, greenhouse gas emissions such as CO₂ and CH₄ dynamics can strongly differ between end-members and transitional thaw stages³⁴.

With permafrost thaw, soils become water-logged and oxygen (O₂) limited, favoring reductive dissolution of reactive Fe(III) minerals¹⁰. Fe(III)-reducing microorganisms are able to use the reactive Fe(III) as an electron acceptor for anaerobic respiration and, depending on its composition, the associated OC as an electron source, resulting in CO₂ and Fe(II) formation³⁵. Thus, Fe(III) reduction directly contributes to CO₂ emissions^{18,35}. Lipson et al.³⁶ previously stated that net reduction of Fe oxides, leading to formation of CO₂, contributes an estimated 40–63% to ecosystem respiration in permafrost environments. Fe(III) reduction may also influence CH₄ emissions in thawing permafrost peatlands: Fe(III) reduction could outcompete methanogenesis³⁷ by being thermodynamically more favorable or in contrast, Fe(III) reduction could favor methanogenesis by leading to proton consumption and thus to an increasing pH³⁸. The complex balance of these processes that either suppress or promote GHG emissions such as CO₂ and CH₄ highlights the need for a fundamental understanding of microbial Fe metabolisms and their interactions with methanotrophs and methanogens, which is currently lacking.

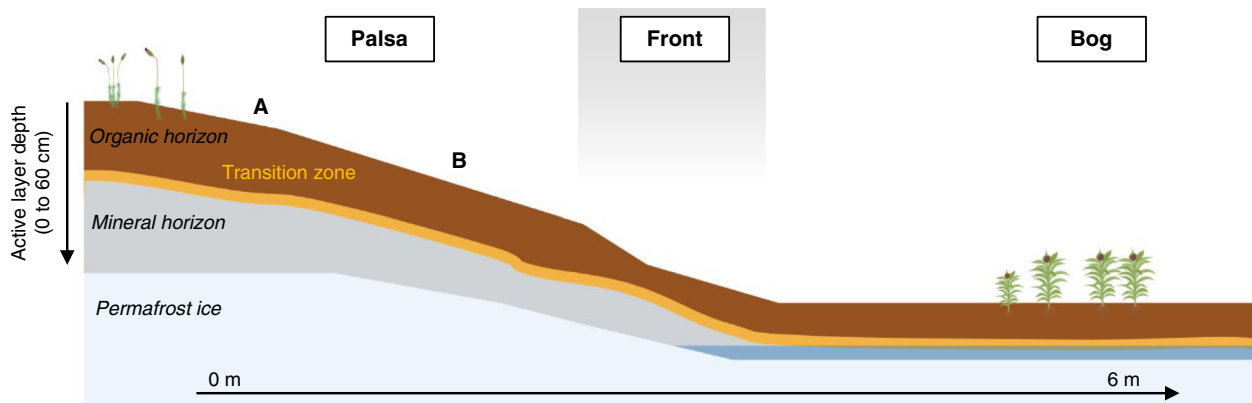
The release of OC previously associated with reactive Fe minerals into surrounding porewater following reductive dissolution could lead to further microbial decomposition of OC and emission of GHGs such as CO₂ and CH₄. Mineral-associated OC (MAOC) has been proposed to be comprised of low molecular weight compounds of microbial (e.g., microbial polysaccharides, amino sugars, muramic acid) and plant origin with low activation energies of MAOC for degradation by microbes^{22,39–42}. Prater et al.⁴² highlighted that the association of OC with mineral surfaces follows the same binding mechanisms as previously described for temperate soils^{13,43}, sorbing OC with similar chemical composition^{12,15,44–47}. The release of MAOC with permafrost thaw is considered as an important driver of the composition of arctic surface waters and microbial respiration^{48–50}. Recent studies described carboxylic-rich⁵¹ and aliphatic Fe mineral-associated OC in forest soils as more resistant to degradation during reductive dissolution⁵². In Siberian permafrost soils, hydrophobic, aromatic DOC was preferentially sorbed by shallower, acidic soil horizons and correlated with an increasing abundance of Fe oxides⁵³. The chemical composition of OC bound to Fe minerals in permafrost environments, however, still remains unknown.

To understand the direct impact of the reductive dissolution of reactive Fe minerals on carbon mobilization and net GHG emissions in thawing permafrost peatlands, it is essential to determine (1) co-occurring greenhouse gas emission patterns, (2) the stability of Fe-OC associations in intact permafrost soils, (3) the potential bioavailability of this Fe mineral-associated OC before and after mineral dissolution and (4) changes in the present and active microbial community which might metabolize OC associated with reactive Fe minerals but also later release OC as greenhouse gases such as CO₂ and CH₄ following permafrost thaw. In particular, the characterization of Fe(III)-reducing bacteria which are key players in reactive Fe mineral dissolution and their interplay with methanotrophs and methanogens is crucial to understand the links between the microbial iron and carbon cycle in thawing permafrost environments.

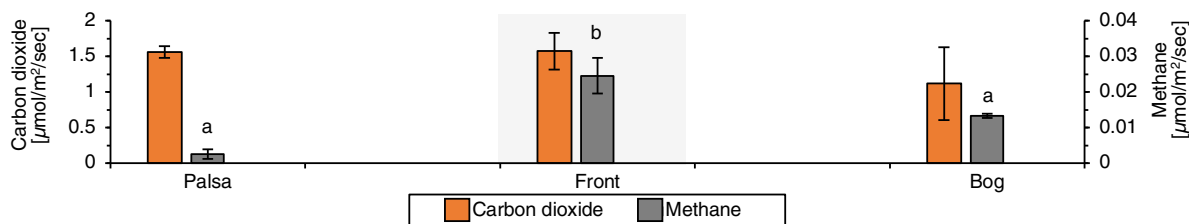
We followed the dynamic biogeochemical interactions of Fe-OC associations in the active layer along collapsing palsa hillslopes, where palsas underlain by intact permafrost with high contents of reactive Fe mineral-associated OC¹⁹ are collapsing into partially-thawed, semi-wet bogs. Fe-OC associations were characterized in the solid phase using selective extractions, scanning electron microscopy (SEM), nanoscale secondary ion mass spectrometry (nanoSIMS), and Mössbauer spectroscopy, and the effect of palsa collapse on porewater geochemistry and CO₂ and CH₄ fluxes was quantified. OC associated with reactive Fe minerals in the solid phase and DOC in the porewater along the palsa hillslope were investigated at the molecular-level with Fourier transform ion cyclotron resonance mass spectrometry (FT-ICR-MS). The present and active microbial community was characterized using DNA- and RNA-based 16S rRNA amplicon (gene) sequencing. All samples were taken during a field campaign in June/July 2019 and thus represent biogeochemical processes in the thawed summer season.

Results and discussion

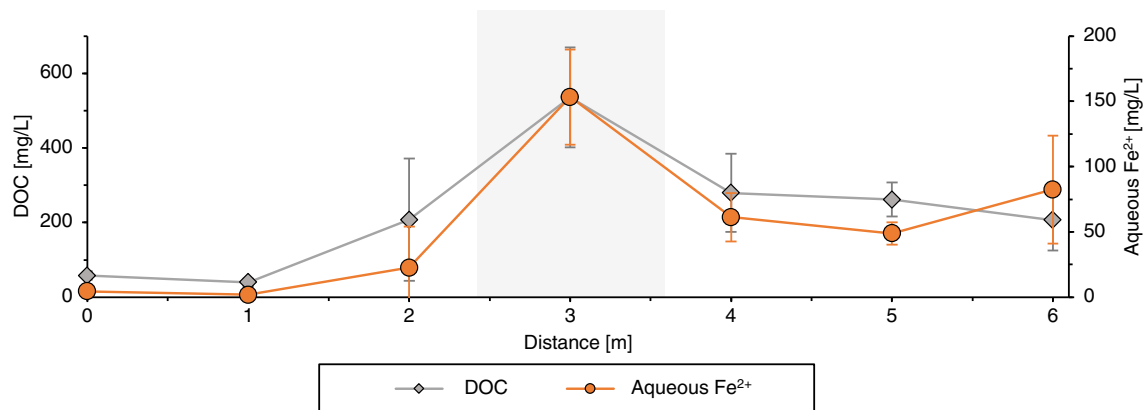
Greenhouse gas emissions promoted by microbial iron cycling in thawing permafrost peatlands. In the palsa and at the collapsing front (Supplementary Figs. S1 and S2), net CO₂ emissions measured from static flux chambers were similar on average ($1.57 \pm 0.27 \mu\text{mol m}^{-2} \text{s}^{-1}$) and slightly decreased in the bog to $1.12 \pm 0.51 \mu\text{mol m}^{-2} \text{s}^{-1}$ (Fig. 1). Replicate analysis of CO₂ concentrations in the automatic Eosense eosFD gas flux chambers showed similar CO₂ emissions along the palsa hillslope (Supplementary Fig. S3). Net CH₄ emissions were very low in the



a Carbon dioxide and methane emissions along the palsa hillslope into bog



b Aqueous Fe²⁺ and DOC pulse along the palsa hillslope into bog



c Relative 16S rRNA gene sequence abundance of iron- and methane-cycling microorganisms from palsa to front

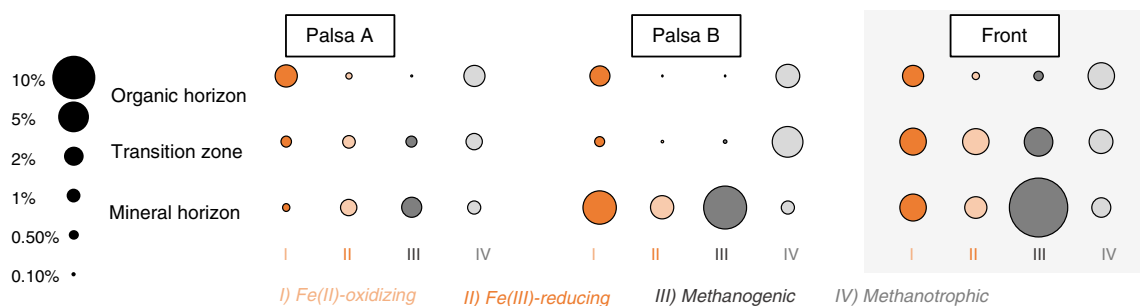


Fig. 1 Microbial iron-cycling and carbon release as dissolved organic carbon (DOC), carbon dioxide and methane emissions along a palsa hillslope.

a Carbon dioxide and methane emissions along the palsa hillslope with highest emissions at the collapsing front. The reported values and error bars represent the average and standard deviation of measurements collected on three days at three separate time points in June/July 2019. **b** Aqueous iron (Fe²⁺) and DOC pulse along the palsa hillslope in the transition zone (interface between organic and mineral horizon, 30 cm depth) with highest values at the collapsing front. Reported values and error bars represent the average and standard deviation of eight palsa to bog hillslopes sampled in June/July 2019. Suprapermafrost water was analyzed in the deeper mineral horizons and cannot explain the pulse of aqueous Fe²⁺ and DOC at the collapsing front (Supplementary Fig. S6). **c** Relative 16S rRNA gene abundance of iron- and methane-cycling strains along the palsa hillslope with highest abundances at the collapsing front: I) Fe(II)-oxidizing, II) Fe(III)-reducing, III) methanogenic and IV) methanotrophic. Small letters above data mean significant differences ($P < 0.05$, one-way ANOVA: TukeyHSD test).

palsa ($0.003 \pm 0.001 \mu\text{mol m}^{-2} \text{s}^{-1}$), increased at the collapsing front to $0.025 \pm 0.001 \mu\text{mol m}^{-2} \text{s}^{-1}$ and then slightly decreased in the bog ($0.013 \pm 0.001 \mu\text{mol m}^{-2} \text{s}^{-1}$; Fig. 1). Emission rates of CO_2 and CH_4 in the palsa and the bog are in line with previous studies at Stordalen mire^{54–56}, however, emissions at the collapsing front, where palsa is collapsing into the bog, have been unknown.

Previous work demonstrated that highest concentrations (mg per g soil) of reactive Fe minerals and associated OC can be found in the zone where the organic and mineral horizons meet, termed the “transition zone”¹⁰. This should not be confused with the layer where active layer meets permafrost, which we do not refer to as the “transition zone” in this case. In the presented study, we focused on the transition zone (interface between organic and mineral horizon) to determine how stable these reactive Fe minerals associated with OC are during palsa collapse. DOC concentrations in the porewater of the transition zone were low in the intact palsa (Palsa A, $58.0 \pm 16.5 \text{ mg L}^{-1}$). Porewater DOC increased towards the collapsing front to $208 \pm 169 \text{ mg L}^{-1}$ in the more collapsed palsa (Palsa B). Highest DOC concentrations were found directly at the collapsing front ($536 \pm 132 \text{ mg L}^{-1}$) and then decreased in the bog (280 ± 113 to $206 \pm 80.3 \text{ mg L}^{-1}$) (Fig. 1, Supplementary Figs. S1 and S4).

The aqueous Fe^{2+} concentrations show the same trend as the DOC (Fig. 1). Aqueous Fe^{2+} concentrations in the palsa were lowest along the palsa hillslope (4.47 ± 3.16 to $22.6 \pm 30.1 \text{ mg L}^{-1}$; Fig. 1) and increased at the collapsing front. Highest aqueous Fe^{2+} concentrations were measured at the collapsing front ($153.2 \pm 40.1 \text{ mg L}^{-1}$) and decreased again at the two measured locations in the bog to 48.9 ± 11.4 and $82.4 \pm 47.9 \text{ mg L}^{-1}$ (Fig. 1). Other elements such as dissolved phosphorous (P) also strongly correlated with the aqueous Fe^{2+} pulse at the collapsing front, suggestive of mineral dissolution and release of mineral-associated P (Supplementary Fig. S5). No aqueous Fe(III) concentrations were detected in the porewater along the palsa hillslope into the bog. Suprapermafrost water (water flowing above the permafrost surface) was present in the deeper mineral horizon and showed no pulse of DOC or aqueous Fe^{2+} at the collapsing front (Supplementary Fig. S6). Generally, palsas and bogs are only fed by precipitation and melt water and have more acidic surface waters (pH ~4). Fens are fed by surface water and groundwater, and maintain slightly acidic to alkaline pH⁵⁷.

The release of OC and aqueous Fe^{2+} along the palsa hillslope was accompanied by an increase in the relative 16S rRNA gene sequence abundance (DNA-based) of iron- and methane-cycling microorganisms in the transition zone and mineral horizon from the palsa to the collapsing front (Fig. 1; Supplementary Fig. S7). Towards the collapsing front, Fe(III)-reducing bacteria increased from 0.41 ± 0.07 to $2.46 \pm 0.34\%$ in the transition zone and from 0.21 ± 0.05 to $2.42 \pm 0.27\%$ in the mineral horizon (Fig. 1). Fe(II)-oxidizing bacteria also increased from the palsa to the collapsing front from 0.54 ± 0.26 to $2.33 \pm 0.33\%$ in the transition zone and from 0.92 ± 0.58 to $1.66 \pm 0.44\%$ in the mineral horizon. Methanogens increased along the palsa hillslope from 0.42 ± 0.37 to $2.83 \pm 0.26\%$ in the transition zone and from 1.40 ± 1.40 to $11.7 \pm 3.12\%$ in the mineral horizon. Methanotrophs increased from the palsa to the collapsing front from 0.90 ± 0.30 to $1.93 \pm 0.09\%$ in the transition zone and from 0.58 ± 0.08 to $1.26 \pm 0.29\%$ in the mineral horizon (Fig. 1). Along the palsa hillslope, the relative 16S rRNA gene sequence abundances of iron- and methane-cycling microorganisms were stable in the organic horizon (Fig. 1). The iron- and methane-cycling microorganisms are described in detail in Fig. 2. For estimated absolute abundances of bacteria and archaea as well as the manually-compiled database used to identify iron- and methane-cycling microorganisms and the whole microbial

community see Fig. 2 and SI (Supplementary Figs. S8 and S9 and Supplementary Tables S1–S4).

This data reveals that reactive Fe minerals are already destabilized during palsa collapse, even before complete permafrost thaw. Lateral flow by runoff of rain and/or melt water^{57,58} in the transition zone between organic and mineral horizon, caused by bulk density shifts (organic horizon: $0.03 \pm 0.01 \text{ g cm}^{-3}$ and mineral horizon: $0.84 \pm 0.26 \text{ g cm}^{-3}$)¹⁰, as also described for other permafrost hillslopes⁵⁹, favors micro-oxic conditions. These micro-oxic conditions favor microbial reduction of reactive Fe(III) minerals coupled to carbon oxidation, as indicated by the high aqueous Fe^{2+} concentrations along the palsa hillslope. Along the thaw gradient, redox potential decreases from $88.8 \pm 4.69 \text{ mV}$ in bog to $-49.3 \pm 1.84 \text{ mV}$ in fen³⁴. These redox conditions promote microbial reduction of reactive Fe(III) minerals coupled to carbon oxidation^{17,36}. This results in a release of Fe and OC that was previously associated with reactive Fe minerals into the surrounding porewater and ultimately contributes to a pulse of aqueous Fe^{2+} and DOC at the collapsing front – where we observed the highest aqueous Fe^{2+} and DOC concentrations ever measured along the whole thaw gradient¹⁰. A simple mass balance approach revealed that reduction of reactive Fe(III) minerals has the potential to release previously associated OC which could account for up to 100% of the measured DOC pulse at the collapsing front (see SI, Supplementary Note 1). However, the release of OC along the palsa hillslope results from multiple co-occurring processes. These include the release of OC associated with reactive Fe minerals, changes in pH⁶⁰, plant community⁶¹ (Supplementary Fig. S10), and in microbial degradation of organic matter⁶².

Although Fe(II)-oxidizers are present and active, they cannot prevent the overall loss of reactive Fe minerals and OC associated with reactive Fe minerals along the palsa hillslope. The CO_2 produced from degradation of released carbon, including OC previously associated with reactive Fe minerals, further stimulated methanogenic microorganisms at the collapsing front. Hydrogenotrophic methanogens for example can use H_2 for the reduction of CO_2 and produce CH_4 in acidic bog peat⁶³.

Abundance of Fe(III)-reducing bacteria increases along the palsa hillslope and we estimate that 22% of CO_2 production could be accounted for by Fe(III) reduction coupled to carbon oxidation (see SI, Supplementary Note 1). Fe(III) reduction coupled to carbon oxidation, leading to direct CO_2 emissions, has also been suggested for subalpine wetland soils⁶⁴ and in arctic peat soils^{17,36}.

Ultimately, the reductive dissolution of reactive Fe minerals, releasing aqueous Fe^{2+} and previously Fe mineral-associated OC into the surrounding porewater, contributes to net GHG emissions of CO_2 and CH_4 , directly by Fe(III) reduction coupled to carbon oxidation and indirectly by promoting methanogenesis at the collapsing front.

Microbial iron- and methane-cycling communities during palsa collapse. Along the palsa hillslope, iron- and methane-cycling microorganisms increase in relative abundance, here defined as DNA-based relative 16S rRNA gene abundance, and in potential activity, here defined as RNA-based relative 16S rRNA abundance (Fig. 2; for total microbial community and replicate analysis see Supplementary Figs. S9 and S11, Supplementary Tables S1–S4).

Fe(III)-reducers, driving reactive Fe mineral dissolution and associated OC release, are found in high abundance and potential activity along the palsa hillslope. From Palsa A to the collapsing front, *Geobacter* spp., a classical Fe(III)-reducer³⁵, increased in relative abundance from 0 to $1.55 \pm 0.30\%$ in the transition zone

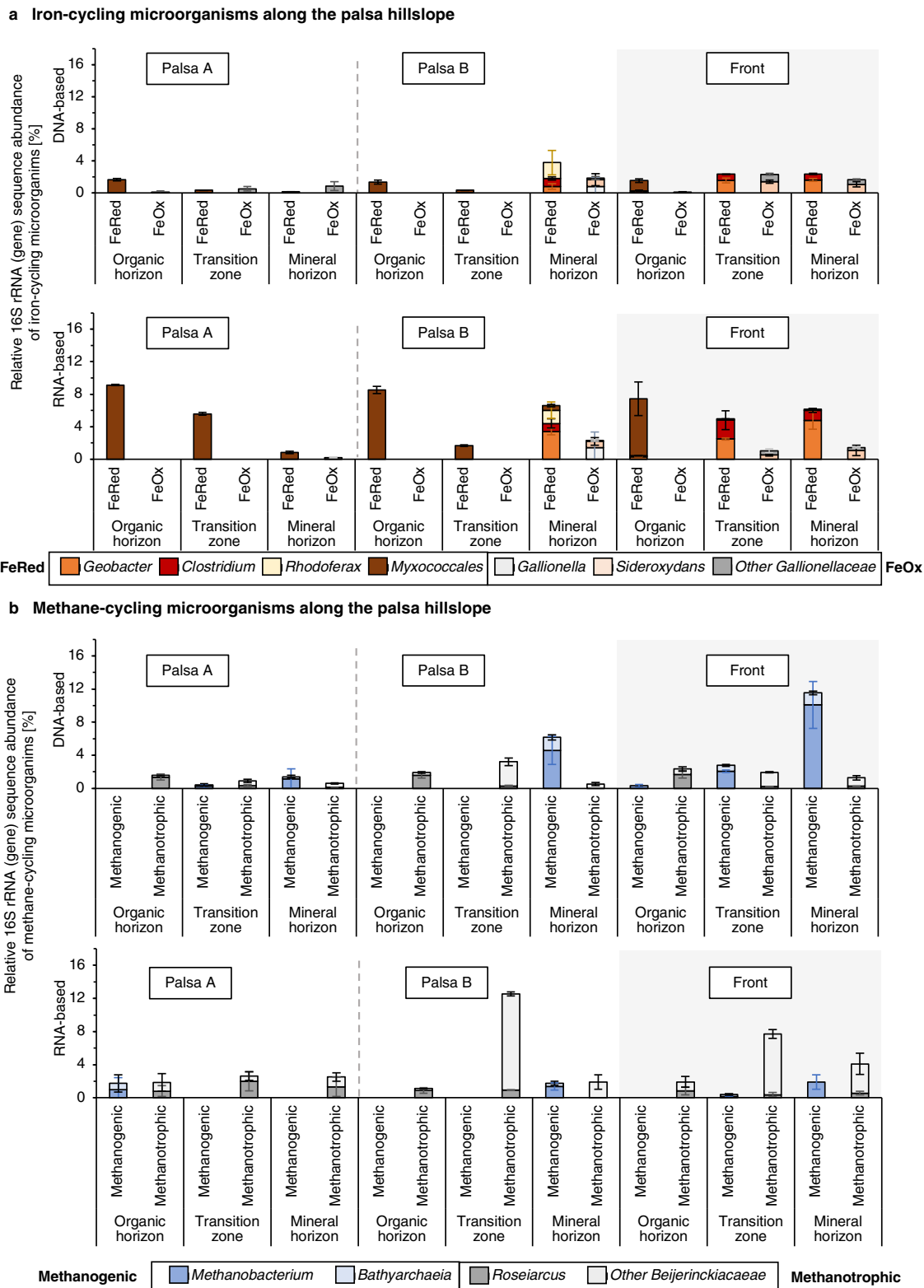


Fig. 2 Relative 16S rRNA (gene) abundance of abundant (DNA-based) and likely active (RNA-based) iron- and methane-cycling microbial communities along the palsa hillslope (Palsa A, Palsa B, Front). **a** Iron-cycling microorganisms show an increasing relative 16S rRNA (gene) abundance (DNA- and RNA-based) along the palsa hillslope with highest abundances in the transition zone and mineral horizon at the collapsing front. **b** Methane-cycling microorganisms are increasing in relative 16S rRNA (gene) abundance along the palsa hillslope. Reported values and error bars represent the average and standard deviation of triplicate analysis of each soil horizon along the palsa hillslope. Replicate cores show similar relative 16S rRNA (gene) abundance of abundant (DNA-based) and potentially active (RNA-based) iron- and methane-cycling microbial communities along the palsa hillslope (Supplementary Fig. S11, Supplementary Tables S1-S4).

and to $1.62 \pm 0.18\%$ in the mineral horizon. The potential activity of *Geobacter* spp. rose from 0 to $2.50 \pm 0.13\%$ in the transition zone and to $4.75 \pm 1.07\%$ in the mineral horizon (Fig. 2). *Clostridium* spp., a fermentative Fe(III)-reducer⁶⁵, increased in relative abundance from 0 to $0.81 \pm 0.02\%$ in the transition zone and $0.76 \pm 0.07\%$ in the mineral horizon (Fig. 2). Potential activity of *Clostridium* spp. increased from 0 to $2.31 \pm 1.15\%$ in the transition zone and to $1.23 \pm 0.22\%$ in the mineral horizon (Fig. 2). *Rhodoferrax* spp., known for dissimilatory Fe(III) reduction¹⁷, only appeared to be present ($1.98 \pm 1.51\%$) and potentially active ($1.62 \pm 0.16\%$) in the mineral horizon of the more collapsed palsa (Palsa B), close to the collapsing front (Fig. 2). *Myxococcales* spp. showed highest relative abundance from $1.67 \pm 0.15\%$ in the intact palsa (Palsa A) to $1.30 \pm 0.23\%$ at the collapsing front and potential activity from 9.13 ± 0.08 in the intact palsa to $7.03 \pm 2.08\%$ at the collapsing front in the organic horizon (Fig. 2).

This microbial community analysis further indicates that the reactive Fe minerals, binding OC, are lost by dissimilatory and fermentative Fe(III) reduction. Dissimilatory Fe(III) reduction is conducted along the palsa hillslope by abundant and active Fe(III)-reducing microorganisms such as *Geobacter* spp., *Rhodoferrax* spp. and *Myxococcales* spp. (Fig. 2; see also absolute abundances in Supplementary Fig. S8 and replicate core analysis in Supplementary Fig. S15)^{66,67}. *Myxococcales* spp. are not only capable of Fe(III) reduction, but also e.g., polysaccharide and protein degradation⁴⁶. *Geobacter* spp. and *Rhodoferrax* spp. represent classical Fe(III)-reducing microorganisms, that are well studied in different environments³⁵ with *Rhodoferrax* spp. also being described at other permafrost sites¹⁷. Fermentative Fe(III) reduction is probably performed by *Clostridium* spp. who might use the present DOC as carbon and energy source.

The abundant and active Fe(III)-reducing bacteria are accompanied by less relatively abundant and probably less active Fe(II)-oxidizers. *Gallionella* spp. had a relative abundance of $0.82 \pm 1.16\%$ in the present microbial community and $1.42 \pm 1.92\%$ in the active community of the mineral horizon of the more collapsed palsa (Palsa B). *Sideroxydans* spp. increased in their relative abundance from below detection to $1.42 \pm 0.21\%$ in the transition and to $1.08 \pm 0.34\%$ in the mineral horizon. Other *Gallionellaceae*, besides *Gallionella* spp. and *Sideroxydans* spp., were equally distributed in their relative abundance along the palsa hillslope from $0.54 \pm 0.26\%$ in the transition zone and $0.86 \pm 0.55\%$ in the mineral horizon of the intact palsa (Palsa A) to $0.90 \pm 0.12\%$ in the transition zone and $0.58 \pm 0.09\%$ in the mineral horizon at the collapsing front. The activity of the other *Gallionellaceae* was probably highest at the collapsing front with $0.53 \pm 0.24\%$ in the transition zone and $0.35 \pm 0.07\%$ in the mineral horizon. The classical Fe(II)-oxidizing bacteria^{66,67} such as *Gallionella* spp. and *Sideroxydans* spp., observed to be present and potentially active in this system were already described in arctic ponds⁶⁸. In this setting, these cannot sustain or reform reactive Fe minerals during palsa collapse (Fig. 2).

The increasing relative 16S rRNA (gene) abundance (DNA- and RNA-based) of classical Fe(III)-reducing bacteria is accompanied by an increase in the relative abundance of methanogenic microorganisms, mainly *Methanobacterium* spp. These increased in their relative abundance in the transition zones from $0.25 \pm 0.24\%$ in the intact palsa (Palsa A) to $2.05 \pm 0.14\%$ at the collapsing front. In the mineral horizon, they rose in their relative abundance from $1.15 \pm 1.22\%$ in the intact palsa (Palsa A) to $10.1 \pm 2.84\%$ at the collapsing front (Fig. 2). Along the palsa hillslope, only a slight increase in potential activity of *Methanobacterium* spp. was observed in the transition zone from 0 to $0.14 \pm 0.05\%$ and in the mineral horizon from 0 to $1.91 \pm 0.85\%$ (Fig. 2). Other methanogens belonging to *Bathyarchaeia* also

increased in relative abundance along the palsa hillslope from $0.17 \pm 0.13\%$ to $0.71 \pm 0.12\%$ in the transition zone and from $0.25 \pm 0.18\%$ to $1.45 \pm 0.24\%$ in the mineral horizon. Methanotrophs, such as *Roseiarcus* spp. and other *Beijerinckiaceae* (i.e., *Methylobacterium* spp. or *Methylocystis* spp.) had an equal relative abundance in the community present along the palsa hillslope (i.e., DNA-based) and had its highest potential activity in the palsa closest to the collapsing front (Palsa B; $12.6 \pm 0.30\%$).

Acetate, formed along the palsa hillslope and accounted for up to $61.7 \pm 42.6 \text{ mg C L}^{-1}$ (10.3% of the total DOC) at the collapsing front. It is expected that this stimulates Fe(III) reduction coupled to acetate oxidation and leads to CO_2 formation by Fe(III)-reducing bacteria such as *Geobacter* spp., known to metabolize acetate³⁵. The potential for reductive acetogenesis from CO_2 by *Bathyarchaeia* was previously suggested⁶⁹. Our MetaCyc ontology predictions showed a high potential for acetoclastic methanogenesis (Supplementary Fig. S12), but contradictory to this, we only saw a high relative abundance of hydrogenotrophic methanogens such as *Methanobacterium* spp. This could be explained by the higher thermodynamic favorability of Fe(III) reduction coupled to acetate oxidation as compared to acetoclastic methanogenesis. Woodcroft et al.⁶² also identified hydrogenotrophic methanogens as being predominantly responsible for CH_4 generation along the thaw gradient.

H_2 and CO_2 , partially produced by fermentation and Fe(III) reduction by e.g., *Clostridium* spp., can be used by hydrogenotrophic methanogens and lead to CH_4 emissions at the collapsing front. Fermentation and acetogenesis by e.g., Acidobacteria or Actinobacteria (also found along the palsa hillslope, Supplementary Fig. S9) were previously identified as essential pathways for degradation of monosaccharides to fermentation products such as ethanol, propionate, acetate and lactate, as well as H_2 and CO_2 along the thaw gradient⁶². The CH_4 is partially oxidized back to CO_2 by methanotrophs as shown by Perryman et al.³⁴ who described highest methane oxidation rates for palsa at the transition between palsa and bog (here referred to as the collapsing front).

Our data clearly shows a co-existence of microbial iron- and methane-cycling microbial communities during palsa collapse, which, together with the present microbial community, ultimately cause GHG emissions and effect the balance between CO_2 and CH_4 emissions even before complete permafrost thaw.

Release of iron-associated organic carbon during palsa collapse. To investigate if the reductive dissolution of reactive Fe minerals and its associated OC also directly contributes to net GHG emissions by releasing potentially bioavailable, previously Fe-bound organic carbon into the porewater, we determined the quantity and identity of Fe-bound OC in the solid phase (defined as dithionite extractable OC) and of the released OC in the porewater. Dithionite did not affect the identity of extractable OC and did not lead to molecular artifact formation (see Supplementary Table S5).

Highest reactive Fe mineral concentrations (defined as Fe reductively dissolved by sodium dithionite and control corrected by leachable Fe, see Methods) were found in the transition zone of the most intact palsa ($10.04 \pm 0.07 \text{ mg reactive Fe minerals per g soil}$; Fig. 3). Towards the collapsing front, reactive Fe minerals in the transition zone between the organic and mineral horizons decreased to $3.22 \pm 0.06 \text{ mg reactive Fe minerals per g soil}$ at the front (Fig. 3). Absolute values are listed in Table S6 and replicate core analysis can be seen in Supplementary Fig. S13. The concentration of OC associated with reactive Fe minerals (OC dissolved after reductive dissolution of reactive Fe minerals by

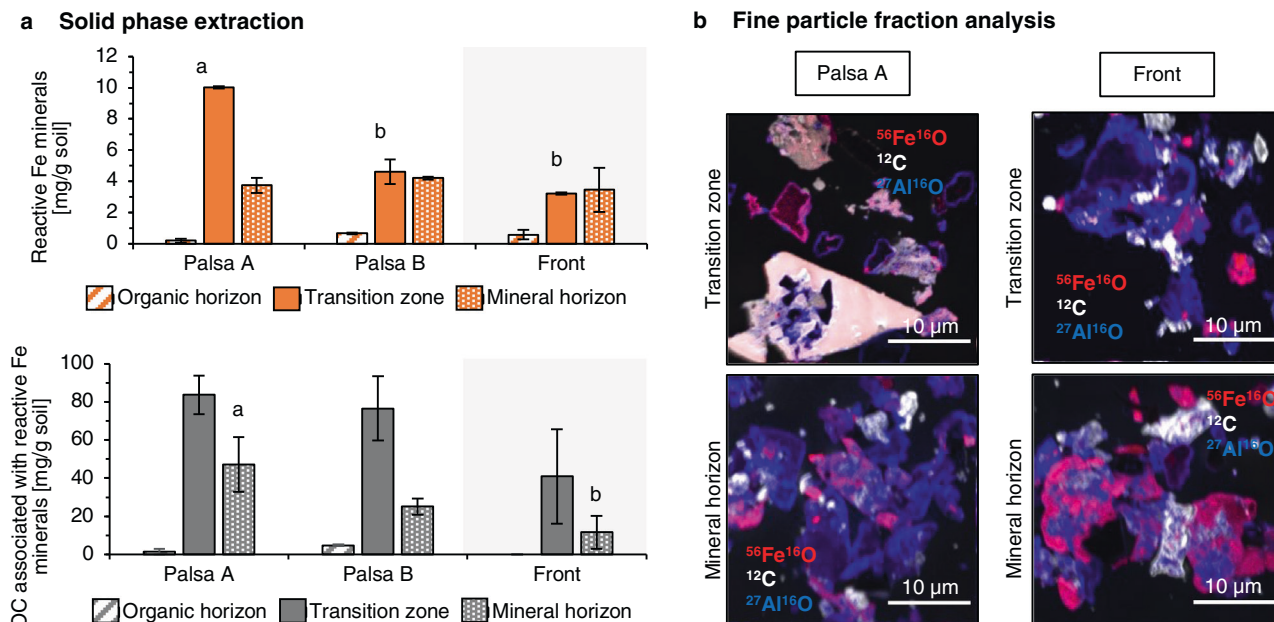


Fig. 3 Reactive iron (Fe) minerals and organic carbon (OC) associated with reactive Fe minerals from intact palsa to the collapsing front. **a** Reactive Fe minerals and associated OC in the solid phase of the bulk soil decrease from the intact palsa (Palsa A) towards the collapsing front. Values of reactive Fe minerals are the average of sodium dithionite citrate duplicate extractions, control corrected by sodium chloride bicarbonate extractable Fe (leachable Fe). Values of OC associated with reactive Fe minerals are the average of sodium dithionite citrate extractions, control corrected by subtraction of the citrate background and the sodium chloride bicarbonate extractable OC (leachable OC) (see Methods). Error bars of reactive Fe minerals represent a combined standard deviation of sodium chloride bicarbonate extractable Fe and sodium dithionite citrate extractable Fe. Errors of the Fe-associated carbon represent a combined standard deviation of the citrate blank, sodium chloride bicarbonate extractable OC and sodium dithionite citrate extractable OC. Different small letters above bars mean significant differences ($P < 0.05$, one-way ANOVA: TukeyHSD test). **b** High spatial resolution analysis of Fe-OC associations by nanoSIMS in the fine particle fraction of the soil, displayed as $^{12}\text{C}^-$ (white), $^{56}\text{Fe}^{16}\text{O}^-$ (red) and $^{27}\text{Al}^{16}\text{O}^-$ (blue) overlaid in a composite image. For the two end-members, Palsa A and collapsing front, four particles of the fine fractions of each layer were analyzed by correlative SEM and nanoSIMS, all showing the same spatial distribution of Fe, C and Al as shown by the four representatives (Supplementary Figs. S14 and S15).

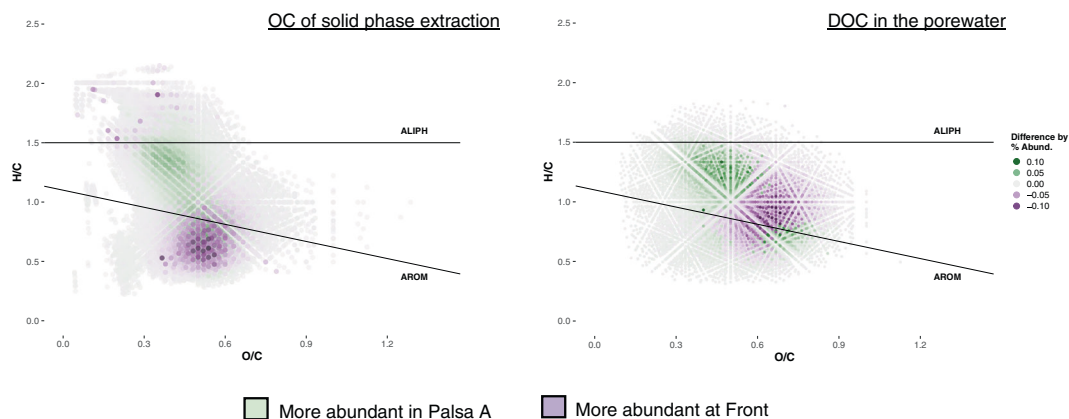
sodium dithionite and control corrected by leachable OC, see Methods) also decreased from the palsa to the bog in the transition zone (83.69 ± 10.04 and 76.60 ± 16.89 mg OC associated with reactive Fe minerals per g soil in the palsa to 40.88 ± 10.76 mg per g soil in the bog) (Fig. 2). It should be noted that TOC is also decreasing from the palsa to the bog in the transition zone (333 ± 21.3 mg TOC per g soil to 57.5 ± 0.38 mg TOC per g soil). In the organic horizons along the palsa hillslope, reactive Fe minerals and associated OC concentrations were the lowest in the soil profile with average values of 0.49 ± 0.25 mg reactive Fe minerals per g soil and 2.08 ± 2.47 mg OC associated with reactive Fe minerals per g soil (Fig. 3). In the mineral horizons from the palsa to the collapsing front, reactive Fe minerals were very stable (average 3.81 ± 0.38 mg reactive Fe minerals per g soil), whereas associated OC slightly decreased from 47.21 ± 14.30 mg OC associated with reactive Fe minerals per g soil in the palsa to the collapsing front which had only 11.60 ± 8.54 mg OC associated with reactive Fe minerals per g soil (Fig. 3). The highest concentration of OC associated with reactive Fe minerals was found in the most intact palsa along the palsa hillslope where Fe was 2-fold higher than Al content (in mg per g soil)¹⁰. This is supported by the strong spatial associations of OC with Fe minerals in the fine fraction observed by nanoSIMS analysis in the transition zone in this core (Fig. 3; see replicate analysis of intact palsa core “Palsa A” in Supplementary Figs. S1, S14 and S15). The transition zone and mineral horizons at the collapsing front showed organic-free, co-existing Fe and aluminum (Al) with similar concentrations (mg per g soil) in the bulk soil¹⁰, suggestive of Fe-bearing clays (Fig. 3). This is also supported by Mössbauer spectroscopy (Supplementary Fig. S16, Supplementary Table S7) and by previous observations with

extended X-ray adsorption fine structure (EXAFS)¹⁰. Future studies should assess the mechanism of inner-sphere interaction (e.g., the identity of complexes formed) between OC and Fe, OC and Al and identify the main organic carbon functional groups (such as C=C, C=O and C–OH) which are co-localized with Fe or Al in the solid phase during permafrost thaw.

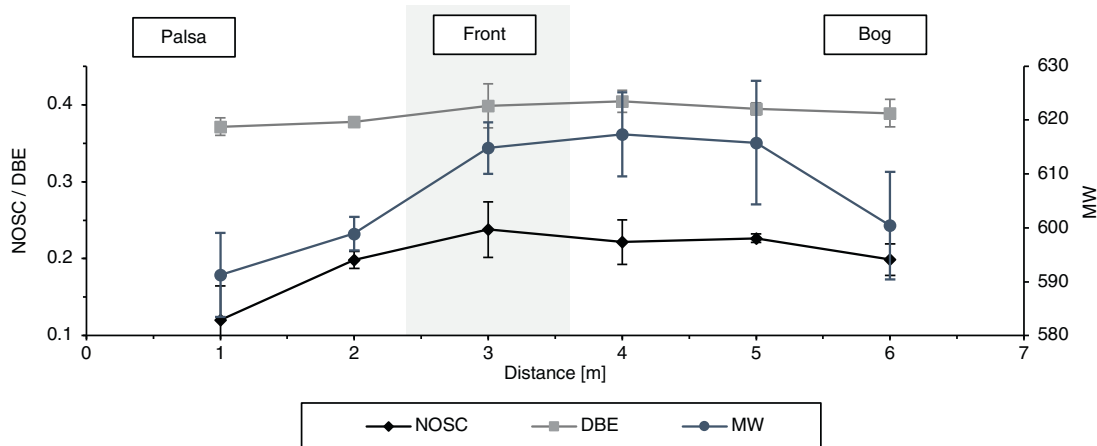
FT-ICR-MS analyses showed that, in the intact palsa, the OC associated with reactive Fe minerals had a higher relative abundance of aliphatic species than the Fe-associated OC at the collapsing front (Fig. 4, un-processed van Krevelen diagrams in Supplementary Fig. S17). This more aliphatic-like fraction could represent amino sugar-like, carbohydrate-like and lignin-like compounds (O/C range: 0.3–0.6, H/C range: 1.0–1.5)^{70,71}. A higher fraction of aromatics was associated with reactive Fe minerals at the collapsing front compared to the organics bound by reactive Fe minerals in the intact palsa (Fig. 4). In general, it should be noted that the concentrations (mg g^{-1}) of OC associated with reactive Fe minerals are decreasing along the palsa hillslope (Fig. 3 and Supplementary Table S5). The higher relative abundance of the more aliphatic compounds associated with reactive Fe minerals in the intact palsa is lost during reductive dissolution to the surrounding porewater along the palsa hillslope, thus the aliphatic fraction most likely contributes to the aqueous Fe^{2+} and DOC pulse at the collapsing front (Fig. 4). Loosely bound OC (salt extractable) appeared in lower quantities and showed less defined but similar identity of organic fractions to the OC associated with reactive Fe minerals (Supplementary Fig. S18, Supplementary Tables S5 and S7).

Porewater extracted from the same soil interface (transition zone), where the reactive Fe minerals and associated OC are lost in the solid phase along the palsa hillslope (Figs. 1 and 2),

a Fate of organic carbon associated with reactive Fe minerals and released organic carbon into the porewater



b Redox properties and molecular weight of released organic carbon into the porewater along the palsa hillslope



c Acetate formation along the palsa hillslope

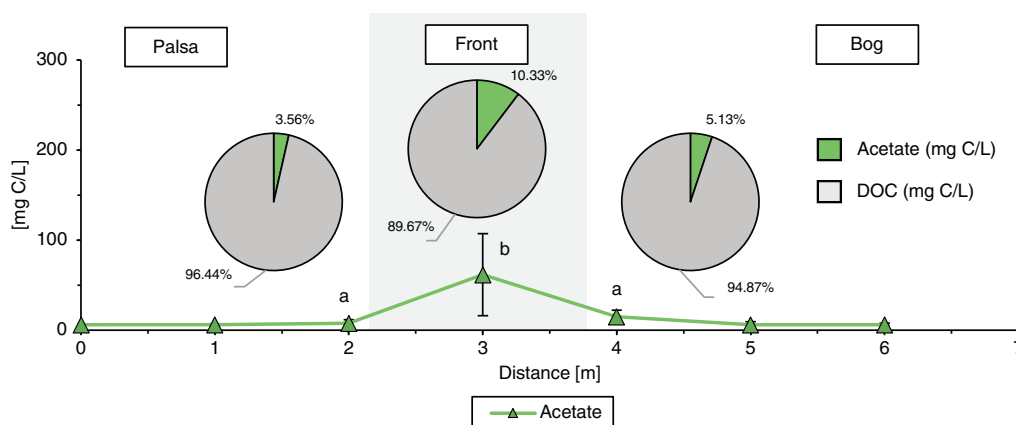


Fig. 4 Bioavailability of reactive iron (Fe)-associated organic carbon (OC) inferred from dissolved organic carbon (DOC) oxidation state and composition. **a** Composition of OC associated with reactive Fe minerals and OC released into the porewater. Fe-bound carbon in palsa soils, underlain by intact permafrost, is comprised of more aliphatic species (class 1, green) and more aromatic species (class 2, purple). This is lost with reductive dissolution into the porewater. Towards the collapsing front into the bog, the remaining OC associated with reactive Fe minerals fraction (purple) is comprised of less bioavailable organic compounds which are likely associated with clay minerals (common in Palsa A, Front and Bog). DOC, which is only found in Palsa A, is enriched in more aliphatic compounds (green). Towards Front and Bog, only more aromatic species (purple) remain (Supplementary Figs. S17–S19, Supplementary Table S5). **b** Redox properties and molecular weight of released organic carbon into the porewater along the palsa hillslope (Supplementary Fig. S20). Reported values and error bars represent the average and the range of duplicate porewater analysis along two palsa hillslopes (Supplementary Figs. S1 and S4). **c** Acetate formation along the palsa hillslope. Following further decomposition of the DOC, highly bioavailable acetate [mg C L^{-1}] is formed which then is again used to further reduce present reactive Fe(III) minerals to Fe^{2+} coupled to acetate oxidation and CO_2 formation. Reported values and error bars represent the average and standard deviation of 8 palsa to bog hillslopes, sampled in June/July 2019 (Supplementary Figs. S1 and S4). Different small letters above data mean significant differences ($P < 0.05$, one-way ANOVA: TukeyHSD test).

contained a higher relative abundance of more aliphatic species and more aromatic species compared to porewater extracted at the collapsing front (Fig. 4; un-processed van Krevelen diagrams in Supplementary Fig. S17). At the collapsing front, an increased relative abundance of organic molecules, potentially representing tannin-like compounds (O/C range: 0.5–0.9, H/C range: 0.5–1.4)^{70,71}, is observed (Fig. 4; Supplementary Fig. S17). The more aliphatic species had a lower relative abundance in the DOC at the collapsing front, whereas a higher relative abundance of more aromatic species was observed (Fig. 4). This could indicate decomposition processes that occur in the palsa hillslope porewater that yield smaller organic compounds, uptake by native microbes, assimilation of organic carbon into biomass and/or further metabolism, and ultimately emissions of GHGs by microbial respiration. Porewater analysis along a replicate palsa hillslope showed the same identity of aliphatic and aromatic species in intact palsa and at the collapsing front (Supplementary Fig. S19).

Further decomposition of DOC along the palsa hillslope is supported by an increasing nominal oxidation state of carbon (NOSC) of the DOC in the porewater at the transition zone from the palsa towards the collapsing front from 0.12 ± 0.04 to 0.24 ± 0.04 (Fig. 4). As the DOC becomes more oxidized, the NOSC increases at the collapsing front. This is in line with an increasing average molecular weight (MW) from 591 ± 7.70 in palsa to 615 ± 0.40 at the collapsing front (Fig. 4b and Supplementary Fig. S20). NOSC values slightly decreased in the bog to 0.20 ± 0.02 due to the overall loss of organic carbon mainly as CO_2 and, consequently, enrichment of less decomposed and more reduced DOC in the porewater. The double-bond equivalents (DBE, the number of rings plus double bonds to carbon, calculated from the neutral elemental composition⁷²), remained stable along the palsa hillslope (0.39 ± 0.08). The DBE along the palsa hillslope showed lower values than previously reported for bog and fen⁶⁰, indicating that bog and fen DOC is overall more unsaturated compared to DOC released along the palsa hillslope.

The further decomposition of released OC contributes to acetate formation (Fig. 4) at the collapsing front, probably by pyruvate fermentation, indicated by MetaCyc ontology predictions (Supplementary Fig. S12). Along the palsa hillslope, acetate in the porewater at the transition zone between organic and mineral horizons significantly increased (unpaired *t*-test, $N = 8$, $\alpha = 0.05$, $p = 0.0024$) from $6.24 \pm 0.34 \text{ mg C L}^{-1}$ (3.56% of the total DOC) in the palsa to $61.7 \pm 42.6 \text{ mg C L}^{-1}$ (10.3% of the total DOC) at the collapsing front, the highest acetate concentrations observed across the whole thaw gradient¹⁰. Further into the bog, the acetate concentrations decreased from 15.1 ± 6.53 to $6.10 \pm 1.44 \text{ mg C L}^{-1}$.

Previous studies at Stordalen mire focused on the soil OC quantity and identity as well as on dissolved organic matter composition (DOM) and DOC transport along the thaw gradient. These analyses have highlighted shifts towards faster decomposition from partially-thawed bog to fully thawed fen with an increasing proportion of carbon released as CH_4 ^{57,60,73}. Processes occurring at the transition between palsa and bog had not been studied, thus enhanced production of acetate and its promotion of methanogenesis at this transition has been overlooked.

Our data showed that reactive Fe minerals at the redox boundary between organic and mineral horizons can bind aliphatic OC, probably by downward cycling of DOM (defined as continuous sorption and precipitation of DOM, as well as of microbial processing, desorption and dissolution proportions of more recent plant-derived compounds^{74,75}) which is released during reductive dissolution into the surrounding porewater. Lower molecular weight compounds, aliphatic compounds or compounds poor in

carboxyl functional groups show lower binding strength to Fe minerals than higher molecular weight compounds, aromatics, or compounds rich in carboxyl functionalities^{74,76}. This is also supported by the leachable OC extractions (same ionic strength and pH as the sodium dithionite extraction; Supplementary Fig. S18). Thus, these compounds are not protected from microbial degradation along the palsa hillslope. The previously Fe-associated aliphatic fraction becomes more bioavailable to microorganisms when it is released from mineral associations⁷⁴. This likely contributes to promotion of microbial growth and respiration of DOM during permafrost thaw^{75,77–79}. Relative to aromatic compounds, aliphatic compounds are expected to be even more labile to microorganisms^{75,77,79}, which is supported by the overall loss of this more aliphatic carbon fraction in the porewater at the collapsing front (Fig. 4) with only minor quantities of aromatic organic molecules remaining preserved by reactive Fe minerals after palsa collapse (Figs. 3 and 4). Kawahigashi et al.⁵³ showed that aromatic DOC was preferentially retained by mineral horizons in Siberian tundra containing reactive Fe.

Our data clearly suggests that the loss of reactive Fe minerals and associated OC via Fe(III) mineral dissolution directly contributes to high DOC concentrations along the palsa hillslope and provides an OC source that is likely more bioavailable than mineral-associated OC thus stimulating microbial respiration and promoting GHG emissions by the present microbial community.

Conclusions and implications for the carbon cycle in thawing permafrost peatlands.

There is a substantial need to piece together carbon sources and sinks in thawing permafrost environments to better understand and quantitatively predict the overall climate impact of permafrost thaw⁸⁰. One such carbon sink or source are Fe-OC associations¹¹, which sequesters OC in intact permafrost soils (up to 20%)^{10,27} but releases it with complete permafrost thaw¹⁰. Our data show that reactive Fe minerals are already reductively dissolved by Fe(III)-reducing bacteria during palsa collapse, releasing aqueous Fe^{2+} and previously associated OC into the surrounding porewater before complete permafrost thaw. The release of the previously Fe mineral-associated OC turns the OC into a source of labile DOC, CO_2 and CH_4 . With increasing abrupt thaw, occurring in 20% of the permafrost zone, new active hillslope features are formed⁸¹ and thus could speed up the loss of reactive Fe minerals via microbial Fe(III) reduction, which at the moment still bind OC in currently intact permafrost environments. Newest estimates showed that collapsing fronts will occupy 3% of abrupt thaw terrain by 2300, but could emit one-third of abrupt thaw carbon losses⁸¹. Ultimately, interlinked processes of iron- and carbon-cycling in thawing permafrost environments need to be integrated into existing climate models to better understand and predict GHG emissions of thawing permafrost areas and thus better estimate its overall climate impact⁸². For this, it is crucial to further determine co-occurring Fe(III) reduction rates and CO_2 and CH_4 production rates following Fe mineral dissolution to quantitatively assess the direct contribution of Fe(III) reduction to ecosystem respiration of CO_2 and CH_4 during permafrost thaw. This includes lab-based experiments which assess the bioavailability of OC associated with reactive Fe minerals, used for Fe(III) reduction by Fe(III)-reducing bacteria, or other present microbial key players (e.g., fermenters), before and after mineral dissolution occurred.

Methods

Site information. Stordalen Mire (68°22' N, 19°03' E) is a subarctic peatland in northern Sweden underlain by discontinuous permafrost. The mire consists of three distinct sub-habitats: (1) palsa (intact permafrost) with ericaceous and woody plants; (2) ombrotrophic peatland or bog (intermediate thaw) with *Sphagnum* spp.,

sedges and shrubs and (3) minerotrophic peatland or fen (fully thawed) with sedges, mainly *Eriophorum spp.*⁶¹. (Supplementary Fig. S1). The areal extent of intact palsa across Stordalen mire has declined significantly since 1970 due to progressive warming in the Arctic, while fen habitats have expanded⁸³. It is also predicted that the whole mire might be free of permafrost as early as 2050^{84,85}.

Gas measurements. To measure CO₂ emissions along the palsa hillslope, two eosense instruments (eosFD Forced Diffusion chamber in conjunction with the eosLink-FD software, EOSENSE INC, Dartmouth, Canada) were installed (Supplementary Figs. S1 and S2): (1) at the top of the palsa hillslope (spot: Palsa A) and (2) at the transition to bog (spot: Front). The collar was situated in a flat location and inserted to near full depth. A centimeter of space was left to aid in installation of the eosFD itself as well as collar retrieval. The collar area was cleared of any rocks or debris, larger vegetation was removed or avoided. The eosFD was deployed in the installed collar. The collars were deployed at least 24 h prior to the start of the eosFD measurement collection to avoid disturbance-related fluxes in the early portion of the data collection. The eosFD samples gases from the atmospheric and soil cavities within the device. Briefly, gas is pulled from the atmospheric cavity to the sensor for 20 s to purge the sensor cavity, then sampled every 10 min for five samples. Gas is then pulled from the soil cavity for 20 sec, then pulsed every 10 min for five samples. Forced diffusion flux is calculated as follows:

$$\frac{V}{A} * \frac{\partial C}{\partial t} = F_s - D \left(\frac{\Delta C}{L} \right)$$

(volume/surface area scaled rate of change in flux rate equal to the flux from the soil surface (F_s) minus the difference in concentration, ΔC (scaled by both the path length L and the diffusivity of the interface (membrane), D)).

The change in the flux rate over the timespan of the concentration measurements (around 60 s) is assumed to be zero (steady state):

$$\frac{V \partial C}{A \partial t} = 0$$

This assumption results in a linear dependence with the path length and interface (membrane) diffusivity being constant and represented by a single coefficient, G:

$$F_s = G \Delta C$$

Furthermore, CO₂ and CH₄ emissions along the palsa hillslope were measured in triplicate using plastic chambers sealed with a rubber stopper (Supplementary Figs. S1 and S2), as described previously⁸⁶. The metal frames were pushed into the ground at least 24 h before the measurements to avoid collecting gas emissions from the soil during installation. Again rocks, debris, and larger vegetation were avoided. Ultrapure water (resistivity of 18.2 MΩ) was used in the frames to seal off the chambers from ambient air. Gas chamber samples were collected with a gas-tight syringe (1100TLL 100 mL Gastight, Hamilton, Reno, NV, USA) and directly transferred into evacuated 12 mL exetainer vials⁸⁷ until analyzed. The sampling was done every 5 min for a total period of 30 mins in duplicates for palsa and front and in triplicates for bog. All gas samples from the field and standard gases used for calibration were measured with a gas chromatograph (Hewlett Packard, 5890 Series II) equipped with an electron capture detector (⁶³Ni-ECD).

Sample collection. In July 2019, cores were taken along three palsa hillslopes (Supplementary Figs. S1 and S7), gently collapsing into bog, following the expected hydrological flow described previously⁵⁷. A Humax corer of 50 cm length and 3-cm diameter with inner liners was used to sample the active layer¹⁰. The inner liners were washed three times with 80% ethanol, six times with sterile MilliQ water, brought into a Biological Safety Cabinet, exposed to UV-light for 15 min and sealed with sterilized butyl rubber stoppers until coring. Butyl rubber stoppers were boiled three times in deionized water and sterilized at 121 °C for 20 min in an autoclave. The cores for mineral analysis were directly split after sampling under 100% N₂ atmosphere in a glove bag and subsamples stored at -20 °C until analysis. The cores for microbial community analysis were split directly in the field wearing gloves that were sterilized with 80% ethanol, immediately frozen with liquid nitrogen and stored at -80 °C until further processing. As previously described¹⁰, the cores were split into three soil horizons based on texture and color changes: (1) A peat or organic horizon, followed by (2) a transition zone between the organic-rich and mineral-rich layer and (3) a mineral horizon.

In July and September 2019, porewater samples were collected from 30 and 60 cm depth below the peat surface along the palsa hillslope (8 transects, Supplementary Figs. S1 and S4) using a luer lock syringe connected to a lysimeter with an effective pore size of 2.5 microns (Simpler Luer-Lock Micro Samplers, Model 1910LL, Soilmoisture Equipment Corp., Santa Barbara, CA). Prior to use, syringes and lysimeters were rinsed 10 times with 50 mL MilliQ water and air dried. Syringe filters (0.22 μm, PES, Merck™ Steritop™, Millipore) were pre-rinsed with 120 mL ultrapure water each to avoid leaching residuals of the filters. The syringes were flushed three times with N₂ and sealed until further use. Syringe filters (0.22 μm) were flushed three times with N₂ and placed into a SCHOTT bottle with N₂ atmosphere until further use. The lysimeters were installed in the soil, pre-flushed by pulling porewater with a syringe and the first 2 mL discharged.

Immediately afterward, the N₂ flushed syringes were unsealed, nitrogen gas pushed out, and then tightly connected to the installed lysimeter. To avoid direct sunlight exposure, syringes were covered with white cotton bags during the time of porewater extraction. After 3-4 h, the samples were filtered through a 0.22 μm syringe filter into stoppered, N₂ flushed glass vials, wrapped in aluminum foil to avoid any sunlight exposure. The first 1 mL filtrate from each sample was disposed. The samples were stored at 4 °C until further analysis.

Selective iron and carbon extractions. To extract reactive Fe minerals and associated OC, selective dissolutions were conducted as described previously¹⁰. Briefly, a sodium bicarbonate (0.11 M) sodium dithionite (0.27 M) trisodium citrate (0.27 M) solution was used to reductively dissolve reactive Fe minerals and release associated OC. As described in Lalonde et al.⁹, a sodium bicarbonate (0.11 M) sodium chloride (1.85 M) solution was used as a control experiment to distinguish between Fe and OC readily desorbed (leachable OC) and OC associated with reactive Fe minerals and only dissolved during reductive dissolution with dithionite. The citrate background in the extract also needs to be subtracted to receive the OC associated with reactive Fe minerals. Thus, only the control corrected values are discussed:

$$\text{Reactive Fe minerals} = \text{Fe(dithionite citrate)} - \text{Fe(sodium chloride)} \quad (1)$$

$$\begin{aligned} \text{OC associated with reactive Fe minerals} &= \text{DOC(dithionite citrate)} \\ &- \text{DOC(blank citrate)} - \text{DOC(sodium chloride)} \end{aligned} \quad (2)$$

For each soil horizon (organic horizon, transition zone, mineral horizon), 0.3 g dry soil was weighed into 10 mL glass vials with 6.25 mL extractant and N₂ headspace. After 16 h at room temperature on a rolling shaker, samples were centrifuged at room temperature for 10 min at 5300 g. The supernatant was decanted and further analyzed for total Fe and DOC.

Geochemical analysis. To determine total Fe and Fe(II), porewater or extract was acidified in 1 M HCl and quantified spectrophotometrically in triplicates with the ferrozine assay⁸⁸. DOC was measured in triplicates with a total organic carbon analyzer (High TOC II, Elementar, Elementar Analysensysteme GmbH, Germany). Inorganic carbon was removed by acidification with 2 M HCl addition prior to analysis. High performance liquid chromatography (HPLC; class VP with refractive index detector [RID] 10 A and photo-diode array detector SPD-M10A VP detectors; Shimadzu, Japan) was used to determine the fatty acid concentrations. To further quantify other elements in the porewater (i.e., phosphorous and sulfur) the samples were acidified in 1% (v/v) HNO₃ and analyzed in triplicates by inductively coupled plasma mass spectrometry (ICP-MS/MS Agilent 8900). A flow injection analysis (FIA) instrument equipped with a dialysis membrane for removal of Fe to prevent side reactions during measurement (Seal Analytical, Germany) was applied for quantification of NH₄⁺, NO₃⁻ and NO₂⁻ concentrations.

Correlative SEM and nanoSIMS analysis. The free particles of the fine fraction of each organic horizon, transition zone and mineral horizon in cores Palsa A (referring to intact palsa), Palsa B (referring to more collapsed palsa) and Front (referring to collapsing front) along the palsa hillslope were analyzed using correlative SEM and nanoSIMS, as described previously^{10,89,90}. Briefly, subsamples of each layer (1 mg) were dispersed in anoxic ultrapure water and reversed for 1 min to obtain the free organo-mineral particles. All larger particles and aggregates were allowed to settle. A drop of 100 μL of the suspension was placed on a silica wafer and dried in an anoxic glovebox (N₂ atmosphere). Finally, samples were sputter-coated with ~30 nm Au/Pd conductive layer using a Bal-Tec SCD005 sputter coater (Baltec GmbH, Germany). To characterize the organo-mineral particles of the fine fraction by size and crystallinity and identify representative particles, a field emission scanning electron microscope (FE-SEM; Jeol JSM-6500F), equipped with secondary electron detector, was used prior to nanoSIMS analysis. The acceleration voltage was set to 5 kV, with a working distance of 10 mm. The nanoSIMS analysis were performed at the Cameca nanoSIMS 50 L of the Chair of Soil Science (TU München, Germany). As described previously¹⁹, a primary ion beam (~2 pA) was set at a lateral resolution ~100 nm and scanned over the samples with ¹²C⁻, ¹⁶O⁻, ¹²C¹⁴N⁻, ³¹P⁻, ³²S⁻, ²⁷Al¹⁶O⁻ and ⁵⁶Fe¹⁶O⁻ secondary ions collected using electron multipliers.

Mössbauer spectroscopy. The soil samples for ⁵⁷Fe Mössbauer spectroscopy were collected under the protection of 100% N₂. Samples from three thaw stages were measured, including Palsa A, Bog and Fen (both wetland cores obtained by a previous campaign see Patzner et al.¹⁰) of transition zone and mineral horizon (Supplementary Fig. S16 and Supplementary Table S7). The samples were dried anoxically before loading into a Plexiglass holder. The prepared samples were stored anoxically at -20 °C until measurement. Mössbauer spectroscopy was performed in a standard transmission setup (Wissel, Wissenschaftliche Elektronik GmbH), and absorption spectra were collected at 77 and 6 K controlling with a closed-cycle cryostat (SHI-850-I, Janis Research Co). The spectra were calibrated with α⁵⁷Fe⁰ foil at 295 K, and fitted using the Voigt Based Fitting (VBF)⁹¹ routine in the Recoil software (University of Ottawa, Canada).

TOC and TN analysis. As described previously¹⁰, total organic carbon (TOC) and total organic nitrogen (TN) were quantified by an Elementar vario El (Elementar Analysensysteme, GmbH, Germany). Soil samples were dried at 60 °C until no further weight loss was observed. The dried soils were ground and acidified with 16% ultrapure HCl to remove the inorganic carbon. After washing with ultrapure water, followed by drying, the TOC and TN content was analyzed. Results of C/N ratios are shown in the SI (Supplementary Fig. S10).

Microbial community analysis. Total RNA and DNA were extracted in triplicates of each soil horizon using the PowerSoil® RNA and DNA isolation kit as described by the manufacturer (MO BIO Laboratories, Carlsbad, CA, USA), with the following modifications: 2–3 g of soil was used per replicate from each soil horizon; 10 min bead-beating; centrifugation steps at maximal speed (7000 × g) at 4 °C; and longer incubation times at –20 °C (1.5 h). RNA and DNA were eluted in 50 µl RNase/DNase-Free water. RNA and DNA concentrations were determined using a Qubit® 2.0 Fluorometer with RNA and DNA HS kits (Life Technologies, Carlsbad, CA, USA). Subsequent DNA digestion and reverse transcription reactions were performed using a Reverse Transcriptase (Invitrogen, Life Technologies) as described previously by Otte et al.⁶⁶. Quantitative PCR (qPCR) specific for the 16S rRNA (gene) of bacteria and archaea was performed as described previously⁶⁶. Microbial 16S rRNA (genes) were amplified using primers 515F and 806R⁹². Quality and quantity of the purified amplicons were determined using agarose gel electrophoresis and Nanodrop (NanoDrop 1000, Thermo Scientific, Waltham, MA, USA). Subsequent library preparation steps (Nextera, Illumina) and sequencing were performed by Microsynth AG (Switzerland) using the 2 × 250 bp MiSeq Reagent Kit v2 on an Illumina MiSeq sequencing system (Illumina, San Diego, CA, USA). From 10,112 to 396,483 (average 113,374) read pairs were generated per sample in three separate sequencing runs on the same MiSeq machine, resulting in total in 8.6 million read pairs. Quality control, reconstruction of 16S rRNA (gene) sequences and taxonomic annotation was performed with nf-core/ampliconseq v1.1.2^{93,94} with Nextflow v2.0.10.0⁹⁵ using containerized software with singularity v3.4.2⁹⁶. Data from the three sequencing runs were treated initially separately by the pipeline using the option “multipleSequencingRuns” and ASV tables were merged. Primers were trimmed, and untrimmed sequences were discarded (<25%, on average 7.7%) with Cutadapt v2.6⁹⁷. Adapter and primer-free sequences were imported into QIIME2 version 2019.10.0⁹⁸, processed with DADA2 version 1.10.0⁹⁹ to eliminate PhiX contamination, trim reads (before the median quality drops below 35, i.e., position 230 in forward reads and 174 in reverse reads), correct errors, merge read pairs, and remove PCR chimeras; ultimately, in total 9,576 amplicon sequencing variants (ASVs) were obtained across all samples. Alpha rarefaction curves were produced with the QIIME2 diversity alpha-rarefaction plugin, which indicated that the richness of the samples had been fully observed. A Naive Bayes classifier was fitted with 16S rRNA (gene) sequences extracted with the PCR primer sequences from the QIIME2 compatible, 99%-identity clustered SILVA v132 database¹⁰⁰. ASVs were classified by taxon using the fitted classifier¹⁰¹. 225 ASVs that classified as chloroplasts or mitochondria were removed, totaling to <7% (average 0.6%) relative abundance per sample, and the remaining 9351 ASVs had their abundances extracted by feature-table (<https://github.com/qiime2/q2-feature-table>).

Pathways, i.e., MetaCyc ontology predictions, were inferred with PICRUST2 version 2.2.0-b (Phylogenetic Investigation of Communities by Reconstruction of Unobserved States)¹⁰² and MinPath (Minimal set of Pathways)¹⁰³ using ASVs and their abundance counts. Inferring metabolic pathways from 16S rRNA amplicon sequencing data is certainly not as accurate as measuring genes by shotgun metagenomics, but it yields helpful approximations to support hypotheses driven by additional microbiological and biogeochemical analyses¹⁰².

FT-ICR-MS analysis. Soil extracts and DOM in the porewater were analyzed with FT-ICR MS to identify and monitor compositional changes in the mineral-associated organic carbon fraction and the mobile, DOC fraction. All of the samples were prepared for FT-ICR-MS analysis by solid phase extraction (SPE) under N₂ atmosphere (glove bag) following the procedure described by Dittmar et al.¹⁰⁴ and Li et al.¹⁰⁵ with some modifications. In brief, 1 g, 3 mL Bond Elut PPL cartridges (part#12102148, Agilent Technologies, Santa Clara, CA, USA) were conditioned with 5 mL of HPLC grade methanol (Sigma-Aldrich, Rehovot, Israel), followed by 5 mL of 0.01 M HCl. Each sample was acidified to pH ~2.5 and then loaded onto the SPE columns, loading volume was adjusted to load a total of 0.5 mg C based on the TOC content. After sample loading, the SPE cartridges were rinsed with 5 mL of 0.01 M HCl followed by drying with N₂ for 3–5 min. Finally, the samples were eluted with 1 mL of HPLC grade methanol and stored in airtight amber sample vials wrapped in aluminum foil at 4 °C. There was no additional dilution of the samples performed prior to analysis by negative ion electrospray ionization.

The samples were analyzed with a custom-built FT-ICR mass spectrometer, equipped with a 21T superconducting solenoid magnet and a modular software package for data acquisition (Predator)¹⁰⁶. Sample solution was infused via a microelectrospray source¹⁰⁷ (50 µm i.d. fused silica emitter) at 500 nL/min by a syringe pump. Typical conditions for negative ion formation were: emitter voltage, –3.0 kV; S-lens RF level, 45%; and heated metal capillary temperature, 350 °C. Ions were initially accumulated in an external multipole ion guide (1–5 ms) and released

m/z-dependently¹⁰⁸. Ions were excited to *m/z*-dependent radius to maximize the dynamic range and number of observed mass spectral peaks (32–64%)¹⁰⁹, and excitation and detection were performed on the same pair of electrodes¹¹⁰. The dynamically harmonized ICR cell in the 21T FT-ICR is operated with 6V trapping potential^{111,112}. Time-domain transients (100 time-domain acquisitions for all experiments) of 3.1 s were acquired with the Predator data station that handled excitation and detection only, initiated by a TTL trigger from the commercial Thermo data station¹⁰⁶. Mass spectra were phase-corrected¹¹³ and internally calibrated with 10–15 highly abundant homologous series that span the entire molecular weight distribution (~150–1300 *m/z*) based on the “walking” calibration method¹¹⁴. Experimentally measured masses were converted from the International Union of Pure and Applied Chemistry (IUPAC) mass scale to the Kendrick mass scale¹¹⁵ for rapid identification of homologous series for each heteroatom class¹¹⁶. Peaks with signal to noise ratios greater than 6 times the noise at the baseline root-mean-square (rms) noise at *m/z* 500 were exported to custom software (PetroOrg®) for additional formula and elemental composition assignment¹¹⁷. All assigned formulas were part of a ≥3 peak carbon series and had less than ±0.3 ppm mass error. A LOD of 6 σ was considered sufficient to minimize ionization difference effects between samples, and therefore biasing by large numbers of low abundance peaks. To further identify macro compositional shifts, analysis of differences between samples was performed only on peaks with ≥20% difference in relative abundance. Additionally, modified aromaticity index (ModAI) was calculated according to Koch&Dittmar⁸⁵ and nominal oxidation state of carbon (NOSC) was calculated according to La Rowe&Van Cappellen¹¹⁸. Data processing post formula assignment was performed with RStudio utilizing R software (V4.0.3).

Statistical analysis. The geochemical parameters were checked with the test of homogeneity. Then a one-way analysis of variance (ANOVA) was used to identify differences in the geochemical parameters along the palsa hillslope, combined with a post-hoc test to identify significant differences between the different sampling spots along the palsa hillslope (from palsa to collapsing front to bog). Based on Gloor et al.¹¹⁹ no statistical analysis (such as e.g., one-way ANOVA or unpaired *t*-test) were chosen for the compositional data obtained by 16S rRNA Amplicon (gene) sequencing.

Data availability

The data that support the finding of this study are included in a compressed Source Data file at Zenodo¹²⁰ (<https://zenodo.org/record/5914518#.Yfe46fvP2Uk>) and raw sequencing data was deposited at the Sequence Reads Archive¹²¹ (SRA, <https://www.ncbi.nlm.nih.gov/bioproject/PRJNA725216>). All FT-ICR MS data (raw files and calibrated peak lists) are available at the Open Science Framework¹²² (<https://osf.io/wts8b/>). Other data are included in the Supplementary Information.

Received: 12 November 2021; Accepted: 24 February 2022;

Published online: 01 April 2022

References

- Ping, C. L., Jastrow, J. D., Jorgenson, M. T., Michaelson, G. J. & Shur, Y. L. Permafrost soils and carbon cycling. *Soil* **1**, 147–171 (2015).
- Hugelius, G. et al. Large stocks of peatland carbon and nitrogen are vulnerable to permafrost thaw. *Proc. Natl Acad. Sci. USA* **117**, 20438–20446 (2020).
- Schuur, E. A. G. et al. Climate change and the permafrost carbon feedback. *Nature* **520**, 171–179 (2015).
- Nowinski, N., Taneva, L., Trumbore, S. & Welker, J. Decomposition of old organic matter as a result of deeper active layers in a snow depth manipulation experiment. *Oecologia* **163**, 785–792 (2010).
- Vonk, J. E. et al. High biolability of ancient permafrost carbon upon thaw. *Geophys. Res. Lett.* **40**, 2689–2693 (2013).
- Henkner, J., Scholten, T. & Kühn, P. Soil organic carbon stocks in permafrost-affected soils in West Greenland. *Geoderma* **282**, 147–159 (2016).
- Hemingway, J. D. et al. Mineral protection regulates long-term global preservation of natural organic carbon. *Nature* **570**, 228–231 (2019).
- Coward, E. K., Thompson, A. T. & Plante, A. F. Iron-mediated mineralogical control of organic matter accumulation in tropical soils. *Geoderma* **306**, 206–216 (2017).
- Lalonde, K., Mucci, A., Ouellet, A. & Gelin, Y. Preservation of organic matter in sediments promoted by iron. *Nature* **483**, 198–200 (2012).
- Patzner, M. S. et al. Iron mineral dissolution releases iron and associated organic carbon during permafrost thaw. *Nat. Commun.* **29**, 6329 (2020).
- Eglinton, T. I. GEOCHEMISTRY A rusty carbon sink. *Nature* **483**, 165–166 (2012).
- Baldock, J. A. & Skjemstad, J. O. Role of soil matrix and minerals in protecting natural organic materials against biological attack. *Org. Geochem.* **31**, 697–710 (2000).

13. Kleber, M. et al. Mineral-organic associations: formation, properties, and relevance in soil environments. *Adv. Agron.* **130**, 1–140 (2015).
14. Kleber, M., Mikutta, R., Torn, M. S. & Jahn, R. Poorly crystalline mineral phases protect organic matter in acid subsoil horizons. *Eur. J. Soil Sci.* **56**, 717–725 (2005).
15. Kogel-Knabner, I. et al. Organo-mineral associations in temperate soils: Integrating biology, mineralogy, and organic matter chemistry. *J. Plant Nutr. Soil Sci.* **171**, 61–82 (2008).
16. Wagai, R., Mayer, L. M., Kitayama, K. & Shirato, Y. Association of organic matter with iron and aluminum across a range of soils determined via selective dissolution techniques coupled with dissolved nitrogen analysis. *Biogeochemistry* **112**, 95–109 (2013).
17. Lipson, D. A., Jha, M., Raab, T. K. & Oechel, W. C. Reduction of iron (III) and humic substances plays a major role in anaerobic respiration in an Arctic peat soil. *J. Geophys. Res.* **115**, G00I06 (2010).
18. Lovely, D. R. & Phillips, E. J. Novel mode of microbial energy metabolism: organic carbon oxidation coupled to dissimilatory reduction of iron or manganese. *Appl. Environ. Microbiol.* **57**, 1536–1540 (1988).
19. Asano, M. & Wagai, R. Evidence of aggregate hierarchy at micro- to submicron scales in an allophanic Andisol. *Geoderma* **216**, 62–74 (2014).
20. Totsche, K. U. et al. Microaggregates in soils. *J. Plant Nutr. Soil Sci.* **181**, 104–136 (2018).
21. Gentsch, N. et al. Storage and transformation of organic matter fractions in cryoturbated permafrost soils across the Siberian Arctic. *Biogeosciences* **12**, 4525–4542 (2015).
22. Gentsch, N. et al. Properties and bioavailability of particulate and mineral-associated organic matter in Arctic permafrost soils, Lower Kolyma Region, Russia. *Eur. J. Soil Sci.* **66**, 722–734 (2015).
23. Herndon, E. et al. Influence of iron redox cycling on organo-mineral associations in Arctic tundra soil. *Geochim. Cosmochim. Acta* **207**, 210–231 (2017).
24. Hobara, S. et al. Geochemical influences on solubility of soil organic carbon in Arctic tundra ecosystems. *Soil Sci. Soc. Am. J.* **77**, 473 (2013).
25. Hobara, S. et al. Relationships among pH, minerals, and carbon in soils from tundra to boreal forest across Alaska. *Ecosystems* **19**, 1092–1103 (2016).
26. Mueller, C. W. et al. Microscale soil structures foster organic matter stabilization in permafrost soils. *Geoderma* **293**, 44–53 (2017).
27. Mu, C. C. et al. Soil organic carbon stabilization by iron in permafrost regions of the Qinghai-Tibet Plateau. *Geophys. Res. Lett.* **43**, 10286–10294 (2016).
28. Borge, A. F., Westermann, S., Solheim, I. & Eitzmüller, B. Strong degradation of palsas and peat plateaus in northern Norway during the last 60 years. *Cryosphere* **11**, 1–16 (2017).
29. Christensen, T. R. et al. Thawing sub-arctic permafrost: effects on vegetation and methane emissions. *Geophys. Res. Lett.* **31**, L04501 (2004).
30. Luoto, M., Heikkinen, R. K. & Carter, T. R. Loss of palsa mires in Europe and biological consequences. *Environmental Conservation* **31**, 30–37 (2004).
31. Olefeldt, D. et al. Net carbon accumulation of a high-latitude permafrost palsa mire similar to permafrost-free peatlands. *Geophys. Res. Lett.* **39**, L03501 (2012).
32. Swindles, G. T. et al. The long-term fate of permafrost peatlands under rapid climate warming. *Sci. Rep.* **5**, 17951 (2015).
33. Shelef, E. et al. Large uncertainty in permafrost carbon stocks due to hillslope soil deposits. *Geophys. Res. Lett.* **44**, 6134–6144 (2017).
34. Perryman, C. R. et al. Thaw transitions and redox conditions drive methane oxidation in a permafrost Peatland. *J. Geophys. Res. Biogeosci.* **125**, G005526 (2020).
35. Kappler, A., et al. An evolving view on biogeochemical cycling of iron. *Nat. Rev. Microbiol.* **19**, 360–374 (2021).
36. Lipson, D. A., Raab, T. K., Gorja, D. & Zlamal, J. The contribution of Fe(III) and humic acid reduction to ecosystem respiration in drained thaw lake basins of the Arctic Coastal Plain. *Global Biogeochem. Cycl.* **27**, 399–409 (2013).
37. Van Bodegom, P. M., Scholten, J. C. M. & Stams, A. J. M. Direct inhibition of methanogenesis by ferric iron. *FEMS Microbiol. Ecol.* **49**, 261–268 (2004).
38. Wagner, R., Zona, D., Oechel, W. & Lipson, D. Microbial community structure and soil pH correspond to methane production in Arctic Alaska soils. *Method Enzymol.* **19**, 3398–3410 (2017).
39. Dao, T. T. et al. Fate of carbohydrates and lignin in north-east Siberian permafrost soils. *Soil Biol. Biochem.* **116**, 311–322 (2018).
40. Evgrafova, A. et al. Small-scale spatial patterns of soil organic carbon and nitrogen stocks in permafrost-affected soils of northern Siberia. *Geoderma* **329**, 91–107 (2018).
41. Mueller, C. W. et al. Large amounts of labile organic carbon in permafrost soils of northern Alaska. *Global Change Biol.* **21**, 2804–2817 (2015).
42. Prater, I. et al. From fibrous plant residues to mineral-associated organic carbon – the fate of organic matter in Arctic permafrost soils. *Biogeosciences* **17**, 3367–3383 (2020).
43. Kleber, M., Sollins, P. & Sutton, R. A conceptual model of organo-mineral interactions in soils: self-assembly of organic molecular fragments into zonal structures on mineral surfaces. *Biogeochemistry* **85**, 9–24 (2007).
44. Christensen, B. T. Physical fractionation of soil and structural and functional complexity in organic matter turnover. *Eur. J. Soil Sci.* **52**, 345–353 (2001).
45. Daugherty, E. E. et al. Hydrogeomorphic controls on soil carbon composition in two classes of subalpine wetlands. *Biogeochemistry* **145**, 161–175 (2019).
46. Sanderman, J., Maddern, T. & Baldock, J. Similar composition but differential stability of mineral retained organic matter across four classes of clay minerals. *Biogeochemistry* **121**, 409–424 (2014).
47. Six, J. et al. Sources and composition of soil organic matter fractions between and within soil aggregates. *Eur. J. Soil Sci.* **52**, 607–618 (2001).
48. Crump, B., Kling, G., Bahr, M. & Hobbie, J. Bacterioplankton community shifts in arctic lake correlate with seasonal changes in organic matter sources. *Appl. Environ. Microbiol.* **69**, 2253–2268 (2003).
49. Judd, K. E., Crump, B. C. & Kling, G. W. Variation in dissolved organic matter controls bacterial production and community composition. *Ecology* **87**, 2068–2079 (2006).
50. Qin, S. et al. Temperature sensitivity of permafrost carbon release mediated by mineral and microbial properties. *Sci. Adv.* **7**, eabe3596 (2021).
51. Zhao, Q. et al. Iron-bound organic carbon in forest soils: quantification and characterization. *Biogeosciences* **13**, 4777–4788 (2016).
52. Adhikari, D. & Yang, Y. Selective stabilization of aliphatic organic carbon by iron oxide. *Sci. Rep. UK* **5**, 11214 (2015).
53. Kawahigashi, M., Kaiser, K., Rodionov, A. & Guggenberger, G. Sorption of dissolved organic matter by mineral soils of the Siberian forest tundra. *Global Change Biol.* **12**, 1868–1877 (2006).
54. McCalley, C. K. et al. Methane dynamics regulated by microbial community response to permafrost thaw. *Nature* **514**, 478–481 (2014).
55. Mondav, R. et al. Discovery of a novel methanogen prevalent in thawing permafrost. *Nat. Commun.* **5**, 3212 (2014).
56. Singelton, C. M. et al. Methanotrophy across a natural permafrost thaw environment. *ISME J.* **12**, 2544–2558 (2018).
57. Olefeldt, D. & Roulet, N. T. Effects of permafrost and hydrology on the composition and transport of dissolved organic carbon in a subarctic peatland complex. *J. Geophys. Res. Biogeosci.* **117**, G01005 (2012).
58. Tang, J. et al. Drivers of dissolved organic carbon export in a subarctic catchment: Importance of microbial decomposition, sorption-desorption, peatland and lateral flow. *Sci. Total Environ.* **622–623**, 260–274 (2018).
59. Lynch, L. M. et al. Dissolved organic matter chemistry and transport along an Arctic tundra hillslope. *Global Biogeochem. Cycl.* **33**, 47–62 (2019).
60. Hodgkins, S. B. et al. Changes in peat chemistry associated with permafrost thaw increase greenhouse gas production. *Proc. Natl. Acad. Sci. USA* **111**, 5819–5824 (2014).
61. Johansson, T. et al. Decadal vegetation changes in a northern peatland, greenhouse gas fluxes and net radiative forcing. *Global Change Biol.* **12**, 2352–2369 (2006).
62. Woodcroft, B. J. et al. Genome-centric view of carbon processing in thawing permafrost. *Nature* **560**, 49–54 (2018).
63. Horn, M. A., Matthies, C., Küsel, K., Schramm, A. & Drake, H. L. Hydrogenotrophic methanogenesis by moderately acid-tolerant methanogens of a methane-emitting acidic peat. *Appl. Environ. Microbiol.* **69**, 74–83 (2003).
64. Pallud, C., Rhoades, C. C., Schneider, L., Dwivedi, P. & Borch, T. Temperature-induced iron (III) reduction results in decreased dissolved organic carbon export in subalpine wetland soils, Colorado, USA. *Geochim. Cosmochim. Acta* **280**, 148–160 (2020).
65. Zhang, Y., Xiao, L., Hao, Q., Li, X. & Liu, F. Ferrihydrite Reduction exclusively stimulated hydrogen production by clostridium with community metabolic pathway bifurcation. *ACS Sustain. Chem. Eng.* **8**, 7574–7580 (2020).
66. Otte, J. M. et al. The distribution of active iron-cycling bacteria in marine and freshwater sediments is decoupled from geochemical gradients. *Method Enzymol.* **20**, 2483–2499 (2018).
67. Weber, K. A., Achenbach, L. A. & Coates, J. D. Microorganisms pumping iron: anaerobic microbial iron oxidation and reduction. *Nat. Rev. Microbiol.* **4**, 752–764 (2006).
68. Emerson, D., Scott, J. J., Benes, J. & Bowden, W. B. Microbial iron oxidation in the Arctic tundra and its implications for biogeochemical cycling. *Appl. Environ. Microbiol.* **81**, 8066–8075 (2015).
69. Loh, H. Q., Hervé, V., Brune, A. Metabolic potential for reductive acetogenesis and a novel energy-converting [NiFe] Hydrogenase in Bathyarchaeia from termite guts - a genome-centric analysis. *Front. Microbiol.* **11** 635786 (2021).
70. Tfaily, M. M. et al. Sequential extraction protocol for organic matter from soils and sediments using high resolution mass spectrometry. *Anal. Chim. Acta* **972**, 54–61 (2017).
71. Tfaily, M. M. et al. Advanced solvent based methods for molecular characterization of soil organic matter by high-resolution mass spectrometry. *Anal. Chem.* **87**, 5026–5215 (2015).
72. McLafferty, F. W., Choi, J., Turecek, F. & Turecek, F. *Interpretation of mass spectra* (University Science Books, 1993).

73. AminiTabrizi, R. et al. Controls on soil organic matter degradation and subsequent greenhouse gas emissions across a permafrost thaw gradient in Northern Sweden. *Front. Earth Sci.* **8**, 557961 (2020).
74. Kaiser, K. & Kalbitz, K. Cycling downwards - dissolved organic matter in soils. *Soil Biol. Biochem.* **52**, 29–32 (2012).
75. Ward, P. C. & Cory, R. M. Chemical composition of dissolved organic matter draining permafrost soils. *Geochim. Cosmochim. Acta* **167**, 63–67 (2015).
76. Curti et al. Carboxyl-richness controls organic carbon preservation during coprecipitation with iron (oxyhydr)oxides in the natural environment. *Commun. Earth Environ.*, **2**, 229 (2021).
77. Abbott, B. W., Larouche, J. R., Jones, J. B., Bowden, W. B. & Balser, A. W. Elevated dissolved organic carbon biodegradability from thawing and collapsing permafrost. *J. Geophys. Res.* **119**, 2049–2063 (2014).
78. Fuchs, G., Boll, M. & Heider, J. Microbial degradation of aromatic compounds - from one strategy to four. *Nat. Rev. Microbiol.* **9**, 803–816 (2011).
79. Mann, P. J. et al. Controls on the composition and lability of dissolved organic matter in Siberia's Kolyma River basin. *J. Geophys. Res.* **117**, G001798 (2012).
80. When permafrost thaws. *Nat Geosci* **13**, 765 (2020). <https://www.nature.com/articles/s41561-020-00668-y#citeas>.
81. Turetsky, M. R. et al. Carbon release through abrupt permafrost thaw. *Nat. Geosci.* **13**, 138–143 (2020).
82. Opfergelt, S. The next generation of climate model should account for the evolution of mineral-organic interactions with permafrost thaw. *Environ. Res. Lett.* **15**, 091003 (2020).
83. Malmer, N., Johansson, T., Olsrud, M. & Christensen, T. R. Vegetation, climatic changes and net carbon sequestration in a North-Scandinavian subarctic mire over 30 years. *Global Change Biol.* **11**, 1895–1909 (2005).
84. Fronzek, S., Carter, T. R., Raisanen, J., Ruokolainen, L. & Luoto, M. Applying probabilistic projections of climate change with impact models: a case study for sub-arctic palusa mires in Fennoscandia. *Climatic Change* **99**, 515–534 (2010).
85. Parviainen, M. & Luoto, M. Climate envelopes of mire complex types in Fennoscandia. *Geogr. Ann.* **A 89a**, 137–151 (2007).
86. Liebner, S. et al. Shifts in methanogenic community composition and methane fluxes along the degradation of discontinuous permafrost. *Front. Microbiol.* **6**, 356 (2015).
87. Glatzel, S. & Well, R. Evaluation of septum-capped vials for storage of gas samples during air transport. *Environ. Monit. Assess.* **136**, 307–311 (2008).
88. Stookey, L. L. Ferrozine - a new spectrophotometric reagent for iron. *Anal. Chem.* **42**, 779–781 (1970).
89. Keiluweit, M. et al. Nano-scale investigation of the association of microbial nitrogen residues with iron (hydr)oxides in a forest soil O-horizon. *Geochim. Cosmochim. Acta* **95**, 213–226 (2012).
90. Kopittke, P. M. et al. Nitrogen-rich microbial products provide new organo-mineral associations for the stabilization of soil organic matter. *Global Change Biol.* **24**, 1762–1770 (2018).
91. Rancourt, D. G. & Ping, J. Y. Voigt-based methods for arbitrary-shape static hyperfine parameter distributions in Mössbauer spectroscopy. *Nucl. Instrum. Methods Phys. Res. Sect. B* **58**, 85–97 (1991).
92. Caporaso, J. G. et al. QIIME allows analysis of high-throughput community sequencing data. *Nat. Methods* **7**, 335–336 (2010).
93. Ewels, P. A. et al. The nf-core framework for community-curated bioinformatics pipelines. *Nat. Biotechnol.* **38**, 276–278 (2020).
94. Straub, D. B. N., Langarica-Fuentes, A., Peltzer, A., Nahnsen, S., Kleindienst, S. Interpretations of environmental microbial community studies are biased by the selected 16S rRNA (gene) amplicon sequencing pipeline. *Front. Microbiol.* **11**, 550420 (2020).
95. Di Tommaso, P. et al. Nextflow enables reproducible computational workflows. *Nat. Biotechnol.* **35**, 316–319 (2017).
96. Kurtzer, G. M., Sochat, V. & Bauer, M. W. Singularity: scientific containers for mobility of compute. *PLoS One* **12**, e0177459 (2017).
97. Martin, M. Cutadapt removes adapter sequences from high-throughput sequencing reads. *EMBnetjournal* **17**, 10–12 (2011).
98. Bolyen, E. et al. Reproducible, interactive, scalable and extensible microbiome data science using QIIME 2. *Nat. Biotechnol.* **37**, 852–857 (2019).
99. Callahan, B. J. et al. High-resolution sample inference from Illumina amplicon data. *Nat. Methods* **13**, 852–857 (2016).
100. Pruesse, E. et al. SILVA: a comprehensive online resource for quality checked and aligned ribosomal RNA sequence data compatible with ARB. *Nucleic Acids Res.* **35**, 7188–7196 (2007).
101. Bokulich, N. A. et al. Optimizing taxonomic classification of marker-gene amplicon sequences with QIIME 2's q2-feature-classifier plugin. *Microbiome* **6**, 90 (2018).
102. Langille, M. G. I. et al. Predictive functional profiling of microbial communities using 16S rRNA marker gene sequences. *Nat. Biotechnol.* **31**, 814–821 (2013).
103. Ye, Y. & Doak, T. G. A parsimony approach to biological pathway reconstruction/inference for genomes and metagenomes. *PLoS Comput. Biol.* **5**, e1000465 (2009).
104. Dittmar, T., Koch, B., Hertkorn, N. & Kattner, G. A simple and efficient method for the solid-phase extraction of dissolved organic matter (SPE-DOM) from seawater. *Limnol. Oceanogr. Meth.* **6**, 230–235 (2008).
105. Li, Y. et al. Proposed guidelines for solid phase extraction of suwannee river dissolved organic matter. *Anal. Chem.* **88**, 6680–6688 (2016).
106. Blakney, G. T., Hendrickson, C. L. & Marshall, A. G. Predator data station: a fast data acquisition system for advanced FT-ICR MS experiments. *Int. J. Mass Spectrom.* **306**, 246–252 (2011).
107. Emmett, M. R., White, F. M., Hendrickson, C. L., Shi, S. D.-H. & Marshall, A. G. Application of micro-electrospray liquid chromatography techniques to FT-ICR MS to enable high-sensitivity biological analysis. *J. Am. Soc. Mass Spectrom.* **9**, 333–340 (1998).
108. Kaiser, N. K. et al. Electrically compensated fourier transform ion cyclotron resonance cell for complex mixture mass analysis. *Anal. Chem.* **83**, 6907–6910 (2011).
109. Kaiser, N. K., McKenna, A. M., Savory, J. J., Hendrickson, C. L. & Marshall, A. G. Tailored ion radius distribution for increased dynamic range in FT-ICR mass analysis of complex mixtures. *Anal. Chem.* **85**, 265–272 (2013).
110. Chen, T., Beu, S. C., Kaiser, N. K. & Hendrickson, C. L. Note: optimized circuit for excitation and detection with one pair of electrodes for improved Fourier transform ion cyclotron resonance mass spectrometry. *Rev. Sci. Instrum.* **85**, 066107 (2014).
111. Boldin, I. A. & Nikolaev, E. N. Fourier transform ion cyclotron resonance cell with dynamic harmonization of the electric field in the whole volume by shaping of the excitation and detection electrode assembly. *Rapid Commun. Mass Spectrom.* **25**, 122–126 (2011).
112. Kaiser, N. K., Quinn, J. P., Blakney, G. T., Hendrickson, C. L. & Marshall, A. G. Novel 9.4 Tesla FT ICR mass spectrometer with improved sensitivity, mass resolution, and mass range. *J. Am. Soc. Mass Spectrom.* **22**, 1343–1351 (2011).
113. Xian, F., Hendrickson, C. L., Blakney, G. T., Beu, S. C. & Marshall, A. G. Automated broadband phase correction of Fourier transform ion cyclotron resonance mass spectra. *Anal. Chem.* **82**, 8807–8812 (2010).
114. Savory, J. J. et al. Parts-Per-Billion Fourier transform ion cyclotron resonance mass measurement accuracy with a “Walking” calibration equation. *Anal. Chem.* **83**, 1732–1736 (2011).
115. Kendrick, E. A. A mass scale based on CH₂ = 14.0000 for high resolution mass spectrometry of organic compounds. *Anal. Chem.* **35**, 2146–2154 (1963).
116. Hughey, C. A., Hendrickson, C. L., Rodgers, R. P., Marshall, A. G. & Qian, K. N. Kendrick mass defect spectrum: a compact visual analysis for ultrahigh-resolution broadband mass spectra. *Anal. Chem.* **73**, 4676–4681 (2001).
117. Corilo, Y. E. PetroOrg Software. (The Florida State University, Tallahassee, FL, USA, 2012).
118. LaRowe, D. E. & Van Cappellen, P. Degradation of natural organic matter: a thermodynamic analysis. *Geochim. Cosmochim. Acta* **75**, 2030–2042 (2011).
119. Gloor, G. B., Macklaim, J. M., Pawlowsky-Glahn, V. & Egozcue, J. J. Microbiome datasets are compositional: and this is not optional. *Front. Microbiol.* **8**, 2224 (2017).
120. Patzner et al. Microbial iron(III) reduction during palusa collapse promotes greenhouse gas emissions before complete permafrost thaw. *Zenodo*. <https://doi.org/10.5281/zenodo.5914518> (2022).
121. 16S rRNA (gene) amplicon sequencing of collapsing palsas, thawing permafrost soils, at Stordalen Mire, Abisko, Sweden in July 2019. Sequence Read Archive. <https://www.ncbi.nlm.nih.gov/bioproject/PRJNA725216>.
122. Open Science Framework Dataset: P18055_Microbial iron(III) reduction during palusa collapse promotes greenhouse gas emissions before complete permafrost thaw. <https://doi.org/10.17605/OSF.IO/WTS8B>. url: <https://osf.io/wts8b/>.

Acknowledgements

We are grateful for assistance in field work and sampling by Sara Anthony and the Arctic Research station (Abisko Sweden), especially Jennie Wikström, Eric Lundin, Niklas Rakos and Alexander Meire, as well as the Swedish Polar Research Secretariat and SITES for the support of the work done at the Abisko Scientific Research Station. We are thankful to Mette Svenning (Arctic University of Norway, Tromsø, Norway) for providing the gas chambers with the plastic lids. We thank EOSENSE INC, Dartmouth, Canada for getting the chance to use the EOSENSE gas chambers for our research. We thank Sara Anthony for analysis of gas samples, Miroslava Malusova and Katrin Wunsch for assistance in the lab, Timm Bayer for his help during SEM analysis and Johann Lugmeier for assistance during nanoSIMS analysis. The authors acknowledge infra-structural support by the Deutsche Forschungsgemeinschaft (DFG, German Research Foundation) under Germany's Excellence Strategy, cluster of Excellence EXC2124, project ID 390838134. This work was supported by the University of Tuebingen (Programme for the Promotion of Junior Researchers award to Casey Bryce) and by the German Academic Scholarship Foundation (scholarship to Monique Patzner). Sara Kleindienst is funded by an Emmy-Noether fellowship from the DFG (grant number 326028733). Daniel Straub was funded by the Institutional Strategy of the University of

Tuebingen (DFG, ZUK63). The National High Magnetic Field Laboratory is supported by the National Science Foundation Divisions of Chemistry and Materials Research through DMR-1644779, Florida State University, and the State of Florida.

Author contributions

The original hypothesis was formulated by M.S.P., C.B. and A.K. M.S.P., C.B. and A.K. designed the project, interpreted the data and wrote the manuscript. M.S.P., C.B. and M.L. collected the samples. M.S.P. and M.L. gathered the data presented in the main text. A.M. conducted the FT-ICR-MS measurements and contributed to the data interpretation. T.B. and R.Y. contributed to the data analysis and interpretation. Z.Z. performed the Mössbauer spectroscopy and helped interpreting the results. H. J helped collecting the porewater samples and data interpretation. C.H. and C.W.M., together with M.S.P., collected, analyzed and interpreted the nanoSIMS data. D.S. processed the amplicon sequencing data and, together with S.K., helped with interpretation of the microbial community results. T.S. contributed to project design and data interpretation. All authors contributed to the preparation of the manuscript and have given approval to the final version of the manuscript.

Competing interests

The authors declare no competing interests.

Additional information

Supplementary information The online version contains supplementary material available at <https://doi.org/10.1038/s43247-022-00407-8>.

Correspondence and requests for materials should be addressed to Casey Bryce.

Peer review information *Communications Earth & Environment* thanks the anonymous reviewers for their contribution to the peer review of this work. Primary Handling Editors: Clare Davis. Peer reviewer reports are available.

Reprints and permission information is available at <http://www.nature.com/reprints>

Publisher's note Springer Nature remains neutral with regard to jurisdictional claims in published maps and institutional affiliations.



Open Access This article is licensed under a Creative Commons Attribution 4.0 International License, which permits use, sharing, adaptation, distribution and reproduction in any medium or format, as long as you give appropriate credit to the original author(s) and the source, provide a link to the Creative Commons license, and indicate if changes were made. The images or other third party material in this article are included in the article's Creative Commons license, unless indicated otherwise in a credit line to the material. If material is not included in the article's Creative Commons license and your intended use is not permitted by statutory regulation or exceeds the permitted use, you will need to obtain permission directly from the copyright holder. To view a copy of this license, visit <http://creativecommons.org/licenses/by/4.0/>.

© The Author(s) 2022